# DATA ANALYSIS AND MATERIAL PROPERTY INFERENCES FROM PASSIVE MICROSCOPIC PROBE EXPERIMENTS IN HETEROGENEOUS BIOLOGICAL SYSTEMS

John Belton O'Neall Caughman III

A dissertation submitted to the faculty at the University of North Carolina at Chapel Hill in partial fulfillment of the requirements for the degree of Doctor of Philosophy in the Department of Mathematics in the College of Arts and Sciences.

Chapel Hill
2023

Approved by:

M. Gregory Forest

David Adalsteinsson

Ronit Freeman

Martin Lysy

Katie Newhall

**ABSTRACT**

John Belton O'Neall Caughman III: DATA ANALYSIS AND MATERIAL PROPERTY INFERENCES FROM PASSIVE MICROSCOPIC PROBE EXPERIMENTS IN HETEROGENEOUS BIOLOGICAL SYSTEMS
(Under the direction of M. Gregory Forest)

Passive particle-tracking microrheology (PPTM) exploits thermal fluctuations of passive microscale probes dispersed in soft matter. The probes are tracked using microscopy; then application of the generalized Stokes-Einstein relation determines the equilibrium dynamic moduli of the sample material. The methodology was designed and applied since the 1990s for presumed homogeneous soft matter materials. The standard PPTM data analysis calculates the ensemble-averaged mean-squared displacement (MSD) of the position time series of tracked particles to determine dynamic moduli of the source material, assuming a faithful random particle sampling of the material. In this dissertation, we confront the challenge of using PPTM to probe heterogeneous materials. Our motivation and the primary application of the tools we develop is the pathology of human airway mucus induced by cystic fibrosis (CF). Normal human bronchial epithelial (HBE) mucus is comprised of a mixture of two large molecular weight mucin polymers, MUC5B and MUC5AC. The mucin ratio of MUC5B:MUC5AC progressively drops during progression of CF, coincident with progressively more extreme heterogeneity in structure whereby the mucin polymers aggregate and phase separate into insoluble, dense flakes within otherwise dilute solutions. These structure properties and the associated heterogeneous rheology are the focus of our analysis. We develop a classifier method based on fractional Brownian motion applied to 200 nm and 1 micron diameter beads that: 1. coarse-grains the particle tracking data into beads within versus outside of flakes; 2. separates within-flake data into increment time series that are distinguishable or not from the noise floor; makes inferences subject to data availability of 3. the heterogeneity in flake structure, 4. the dynamic moduli of flakes and of the dilute solution as inferred from both probe diameters.

## ACKNOWLEDGMENTS

Partial support for John Caughman is gratefully acknowledged from the National Science Foundation, award NSF-DMS-1929298 to the Statistical and Applied Mathematical Sciences Institute.

## TABLE OF CONTENTS

## LIST OF FIGURES

## LIST OF TABLES

CHAPTER 1

# Introduction

In the human body, mucus is an intrinsic part of many organ systems, including the gastrointestinal[Allen (1993)], respiratory [Silberberg (1982), and reproductive [Katz (1982)] tracts. All of these types of mucus are made up of a mucin polymer network at the molecular level, with the make-up differing in chemical makeup between organ systems allowing for a difference in barrier and flow properties. With disease conditions, such as cystic fibrosis (CF), chronic obstructive pulmonary disease (COPD), and stomach ulcers, a breakdown in the normal functional behavior of mucus develops. We do not focus on the cause of this functional disruption, rather we focus on the detection of departure from normal structure and rheology, and heterogeneity in particular.

Typical healthy mucus is composed of 90-98% (by mass) of water, 2-5% mucins, 1-2% lipids, 1% salts, and a very small % of DNA fragments and other molecular species [Thornton (1982)]. In Hill (2014), the mucus solids concentration from sputum, a mixture of saliva and mucus from the respiratory tract, is measured, revealing weight percents of 1-2% for normal sputum, 2-6% for COPD sputum, and 5-9% for cystic fibrosis sputum. The physical properties of the mucus are generally defined by the entanglement of mucins with one another and other molecules to form a three-dimensional network or gel-matrix. This creates a medium that exhibits viscoelastic properties, i.e., they have both the viscous properties of a liquid as well as the elastic properties of a solid. Mucus both traps and transports all inhaled insults, and the viscoelastic properties are tuned to achieve both functionalities. Due to low volume and yield thresholds, particle-tracking microrheology (PPTM) allows for the most viable and robust assessment of rheological properties. In PPTM, [Mason (1995, 1997, 2000)], microbeads are embedded in a sample and their positions recorded without any external forces being applied. This results in a position times series,

$$\{X_n = X(n \cdot \tau), n = 0, 1, ...N\}$$

being recorded using particle-tracking microscopy, where $\tau = \Delta t$ is the experimental lag time between

recorded positions of the microscope, and $\tau \cdot N$ is the total tracking time; $\tau$ and N are uniform across tracked beads for statistical robustness of data inference. From the time series data, one then calculates increment statistics, specifically the time-averaged mean-squared-displacement of each tracked bead, $MSD_X$, computed for all lag times $n\tau$:

$$MSD_X(n\tau) = \frac{1}{N-n-1}\sum_{j=0}^{N-n} ||X_{n+j} - X_n||^2 \tag{1.1}$$

Positions $X_j$ have dimension $d$, where typically $d = 2$ with beads tracked in the focal plane of the microscope.

The pure, medium-induced, increments and MSD statistics, i.e. free from experimental noise and tracking error, are inserted into the Generalized Stokes-Einstein Relation (GSER), mapping from experimental lag times to frequency, $n\tau = \frac{1}{\omega}$. The GSER can be applied to data of individual tracked beads of radius r, Equation (1.2) below, or for ensemble-averaged MSD statistics, Equation (1.3). The elastic, $G'(\omega)$, and viscous, $G"(\omega)$, dynamic moduli of the medium surrounding individual beads (1.2) or a randomly sampled medium (1.3) are given by:

$$G^*(\omega) = G'(\omega) + iG"(\omega) = \frac{k_B T}{\pi r i\omega \mathfrak{F}(MSD_X(n\tau))} \tag{1.2}$$

$$G^*(\omega) = G'(\omega) + iG"(\omega) = \frac{k_B T}{\pi r i\omega \mathfrak{F}(\langle MSD_X(n\tau)\rangle)} \tag{1.3}$$

where $\mathfrak{F}(\cdot)$ is the Fourier transform. Equation (1.3) is the standard formula employed for presumed homogeneous materials, where $\langle\cdot\rangle$ denotes the ensemble average over all tracked beads. This methodology has been indispensable for soft complex fluids with extremely low yield thresholds and low volume availability. Human bronchial epithelial (HBE) mucus meets both of these criteria (cf. Fahy (2000); Bansil (2018); Wagner (2018); Boucher (2019)), and passive particle-tracking microbead rheology has emerged as the method of choice Crater (2010); Hill (2014); Lysy (2016); Wagner (2017); Hill (2018); Newby (2018).

As noted, we focus on challenges in PPTM with pathological mucus, marked by extreme heterogeneity, that develops during progression of cystic fibrosis [Hill (2018), Esther (2019), Ford (2021)]. In addition to previously documented increases in mucus concentration [Hill (2014)], CF HBE mucus undergoes a heterogeneous phase transition [Markovetz (2019), Markovetz (2022)]: dense, raft-like, structures, referred to as flakes, self-assemble and phase separate from the remaining more dilute solution. In advanced stages of CF, up to $50\%$ of the mucin polymers (MUC5B and MUC5AC) in HBE mucus phase-separate into highly

concentrated flakes that do not swell nor dissolve in airway surface salt-water solvent. Advanced CF HBE mucus is thereby, at a coarse scale, a two-phase mixture: a dense phase of mucin flakes, and a more dilute phase consisting of the remaining mucins in dilute solution. Additional scales of spatial heterogeneity potentially exist within the two coarse phases for any given sample: the dilute phase may vary in mucin concentration; flake lateral dimensions range from 1-100 microns, with unknown free-volume pore-size distributions that govern admissibility of passive probes added to samples. The goals are to infer heterogeneity of progressive CF mucus, first at the coarse scale of two phases (flakes, not flakes), second to explore evidence of heterogeneity especially within flakes, and third to use the appropriate GSER to link dynamic moduli with structure heterogeneity. A secondary goal is to determine if these layers of heterogeneity are statistically distinct at 200 nm and 1 micron probe diameters. Care is taken in experiments to limit the number of beads in HBE samples to avoid creation of a complex colloid.

PPTM data of flake-prevalent samples poses new data-analysis challenges that must be resolved and implemented. A statistically robust and accurate method is presented that does the following: (1) separates beads for each sample into within-flakes versus outside-flakes; (2) for within-flake beads, determines which data are distinguishable from immobilized or stuck bead data of the same microscope system; (3) for within-flake beads distinguishable from the noise floor, disentangles the pure entropic medium signal from experimental error and noise. For all measured time series data distinguishable from the noise floor, a 2-parameter classifier of the pure entropic mean-squared displacements (MSD) is developed, described below.

Heterogeneity, low bead sample sizes, and unknown sampling efficacy of the heterogeneous domains combine to impose hard constraints on the form of the Generalized Stokes-Einstein Relation (GSER) one should use, and limit what one is capable of inferring with respect to rheology. In particular, ensemble averaging of bead MSDs in the GSER is justified by an ergodicity assumption for homogeneous materials, such that ensemble averaging of bead MSDs in the time domain is equivalent to frequency-domain averaging of the Fourier-transformed MSDs, and that the beads give a random and sufficient sampling of the material. These assumptions are egregiously violated for flake-prevalent mucus [Markovetz (2019), Markovetz (2022)].

We begin with the following assertion: any characterization of heterogeneity, i.e., some metric to cluster the total ensemble of tracked bead position time series, should be implemented on the primitive data, namely the measured position increment time series. Clustering of the data should not be performed in the frequency domain of viscoelastic moduli, which involves a nonlinear mapping of the primitive data: a Fourier transform of the increment time series data to the frequency domain and then the reciprocal of the transform inserted into

the GSER formula (2) or (3). The heterogeneity method presented here is implemented on the 2-parameter MSD classifier per bead time series and then the ensemble of tracked bead classifier data per mucus sample. In the 2-parameter MSD classifier space for each mucus sample and for each bead diameter, 3 clusters are identified: (1) beads outside of flakes in relatively dilute mucus with water-like signals; (2) beads within flakes whose entropic fluctuations are indistinguishable from the noise floor; and (3) beads within flakes whose pure entropic fluctuation signal are distinguishable from the noise floor. The GSER is then applied to the individual bead MSD classifier data, and the cluster results are leveraged to reveal the distribution of dynamic moduli from available beads within and outside of flakes. Furthermore, while no moduli inferences of within-flake beads inside the noise floor are made, inferences about flake pore sizes based on total bead numbers within flakes for 200 nm versus 1 micron diameter beads relative to the expected numbers on the basis of relative bead mobility and flake encounter frequency are done.

One final issue is efficacy of the MSD classifier, which is independently tested from the experimental truth data. Each video is analyzed and the spatial proximity of beads within versus outside of individual flakes are attached. In doing so, we confirm quite high success rates; for apparently misclassified beads, we find those beads appear to be weakly within the focal plane. In the absence of such experimental truth sets, such errors could be lessened by filtering tracked beads with low signal to noise ratio, SNR, below a threshold set by the imaging system.

For all data distinguishable from the noise floor, a predictor-corrector method is introduced to extract the pure entropic fluctuation signal. The predictor step is a least-squares fit to the drift-subtracted MSD on a restricted range of lag times that mitigates high frequency error (dynamic and static) and drift-subtracted distortion at large lag times. The corrector step is the fractional autoregressive moving average (fARMA) method of high-frequency noise removal developed in [Lysy (2016)]. The predictor step was formulated precisely for these heterogeneous HBE mucus samples to avoid instability of fARMA from initial guesses outside the range of convergence to the true MSD. The predictor-corrector method yields the 2-parameter classifier of the purely entropic, medium-induced, sub-diffusive MSD over measured timescales. Later in this work, the method is applied on synthetic, simulated data, revealing estimators and standard errors across ranges of truth datasets over a range of Brownian and sub-diffusive processes, with superposition of various combinations of experimental error. The results show potentially major errors arise for low-mobility increment time series by using a least-squares fit to the MSD, even if one restricts the window to avoid low and high frequency noise. The take-home message here is that one cannot avoid the pollution of the MSD at

intermediate timescales due to noise outside the restricted window.

### 1.1 Particle position time series data and statistical analysis of the data

Recall equation (1.1) that describes the MSD per lag time, $n\tau$. For a spherical particle of radius r diffusing in a purely viscous medium, e.g., water or glycerol of viscosity $\eta$, the position time series is described by Brownian motion, for which the MSD scales linearly for all lag times:

$$MSD_X(n\tau) = 2dDn\tau \tag{1.4}$$

where d is the dimension of the trajectory and D is the diffusivity of the medium given by the Stokes-Einstein relation,

$$D = \frac{k_B T}{6\pi r \eta} \tag{1.5}$$

Soft biological materials like mucus are both viscous and elastic, with different responses at different frequencies of forcing. In viscoelastic materials, the MSD of passive beads is sub-linear over the timescales for which the medium exhibits memory due to elastic recoil of the polymeric network. For 200 nm to 1 micron diameter passive beads in respiratory mucus, and for our microscope system, the memory timescales encompass the camera shutter timescale (1/60 sec) and the total bead observation time (30 sec). Furthermore, over experimental timescales, each individual tracked bead not in pure salt-water exhibits a sub-diffusive MSD power law,

$$MSD_X(n\tau) = 2dD_\alpha(n\tau)^\alpha \tag{1.6}$$

for $0 < \alpha < 1$. The only Gaussian continuous stationary increments (CSI) process having this power law MSD at all time scales is fractional Brownian motion $B_\alpha(t)$, of which the auto-correlation function is

$$E[B_\alpha(t), B_\alpha(s)] = \frac{1}{2}(|t|^\alpha + |s|^\alpha - |t-s|^\alpha)$$

It is important to emphasize that the statistical classifier for Brownian motion is one-dimensional, the diffusivity D, whereas for sub-diffusive fractional Brownian motion, the classifier is two-dimensional, $(\alpha, D_\alpha)$. The power law $\alpha$ reflects the degree of sub-diffusivity of the medium surrounding each tracked particle, where an $\alpha$ around 1 is close to pure diffusion while an $\alpha$ value near 0 corresponds to almost complete immobility. The pre-factor $D_\alpha$, however, has $\alpha$-dependent units, so that one cannot compare numerical values of different

beads unless they miraculously have identical $\alpha$, nor can one perform arithmetic operations (e.g., averaging) over ensembles of tracked particles. In particular, one cannot employ clustering metrics, and therefore we are unable to assess heterogeneity. This issue will be resolved in a later discussion. For now, it can be noted that

$$\Delta = 2dD_\alpha(n\tau)^\alpha = \text{MSD}_X(n\tau \text{ sec}), \tag{1.7}$$

for any lagtime $n\tau$, e.g. $n\tau = .1$ or 1 seconds, has units $\mu m^2$ and therefore can be readily compared across multiple beads and used for averaging or cluster analysis. Alternatively, one can also use the GSER per bead and compare the dynamic moduli G' and G" of different tracked beads at any frequency, e.g., 10 or 1 $\text{sec}^{-1}$, or perform other statistical analyses. *The problem* with any of these single lagtime or frequency projections onto a scalar quantity *arises when the bead time series data has not been denoised first* – the potential for error is exaggerated for the highly sub-diffusive time series of beads inside flakes.

If one assumes that the MSD classifier $(\alpha, D_\alpha)$ is a denoised projection onto fractional Brownian motion (fBm), *the classifier further provides an analytical formula for the dynamic modulus by virtue of the exact Fourier transform of the power-law MSD* (1.6), *avoiding numerical error*:

$$i\omega\mathfrak{F}(2dD_\alpha(n\tau)^\alpha) = \Gamma(1+\alpha)6D_\alpha\left(\frac{1}{\omega}\right)^\alpha i^{-\alpha} \tag{1.8}$$

Using this exact formula in the GSER, equation (1.2), for each individual bead:

$$G^*(\omega) = \omega^\alpha\left[\frac{k_BT\cos(\frac{\alpha\pi}{2})}{\pi r\Gamma(1+\alpha)6D_\alpha}\right] + i\omega^\alpha\left[\frac{k_BT\sin(\frac{\alpha\pi}{2})}{\pi r\Gamma(1+\alpha)6D_\alpha}\right] = G'(\omega) + iG"(\omega) \tag{1.9}$$

where $\Gamma(\cdot)$ is the Gamma function. From the ensemble of bead classifiers per sample per experiment, after appropriate rescaling of $D_\alpha$ to perform clustering, beads are filtered into two stages: tracked beads outside flakes with a water-like signal and tracked beads within flakes with a highly sub-diffusive signal. Then within flake beads are filtered into time series distinguishable from the noise floor determined by tracking of stuck beads and those inseparable from the noise floor. We find that the successfully denoised coarse clusters, outside and within flakes, are sufficiently separated to be robust. This point is illustrated with synthetic data in Figure 1.1.

*Figure 1.1, left and middle panels, illustrate equivalence of using forms (2) and (3) of the GSER for homogeneous clusters*. The left panel data mimics water-like signals in dilute HBE mucus and the middle

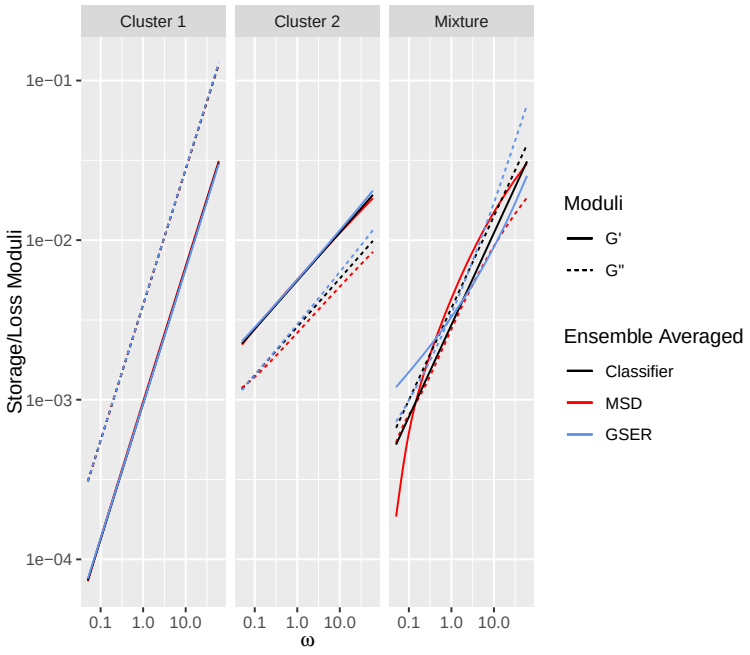


Figure 1.1: Comparison between G' and G" computed three ways: (1) GSER applied to denoised MSD classifier $(\alpha, D_\alpha)$ per bead, eqn 1.2, then averaging G and G in frequency space; (2) ensemble averaging over all denoised bead MSDs, then apply GSER, eqn 1.3 ; (3) ensemble averaging of the denoised MSD classifiers, giving a mean $(\alpha, D_\alpha)$, therefore a denoised power law ensemble-average MSD, inserted into either eqn 1.2 or eqn 1.3. These approaches are implemented for two separate homogeneous clusters: a water-like cluster on the left, cluster 1, and a flake-like cluster in the middle, cluster 2, illustrating consistency in the approaches for homogeneous clusters. The mean dynamic moduli of the mixture of these two clusters are computed with each approach on the right, showing inconsistency in the approaches for heterogeneous clusters.

panel mimics flake-like signals, both drawn from a normally distributed mean MSD classifier $(\alpha, D_\alpha)$. (To do this, a consistent dimensional or non-dimensional scalar for all tracked beads, e.g., equation (1.7) is extracted from $D_\alpha$, then draw from a normal distribution, and then pass back to $D_\alpha$.) For the water-like signal the chosen mean and standard deviation for $(\alpha, \widetilde{D}_\alpha)$ are, $\mu = (0.85, 0.35)$ & $\sigma = (0.03, 0.02)$, while for the flake-like signal $\mu = (.3, .15)$ & $\sigma = (0.07, 0.02)$. While these clusters are not homogeneous in the strict sense, having identical $(\alpha, D_\alpha)$ values for every particle in the cluster, but rather in the broader sense of having some variation of these parameters that is consistent with that observed in empirical data we deem to be homogeneous from a practical standpoint. The standard deviation for the $\alpha$ value in the water-like signal is smaller to ensure that all $\alpha$ remain less than one, i.e., are sub-diffusive, since $\alpha > 1$ causes anomalous G $<$ 0 and a misleading ensemble average. These $(\alpha, \widetilde{D}_\alpha)$ distributions were chosen independently due to lack of knowledge of their correlations. The right-most panel shows the non-equivalence of the three methods for averaging of tracked bead data in a heterogeneous mixture of these two normally distributed water-like and

bead-like clusters. In both homogeneous clusters all three approaches recover a power-law rheology scaling, i.e., approximately linear in log-log space, whereas only approach (3) is guaranteed to give power-law scaling. For the heterogeneous mixture in the right panel, methods (1) and (2) produce a non-power law scaling of G', G", distinct from method (3). Neither of the methods for the heterogeneous mixture on the right-most panel has meaningful physical relevance: they average over the underlying heterogeneity without knowledge of volume fractions of flakes and dilute solution and proper weighting of each in the average, and evidence exists that the transport properties of the mixture are nonuniform between the flakes and dilute solution.

CHAPTER 2

# Estimating Diffusion Parameters

## 2.1 Semiparametric Least-Squares Estimator

Least squares is the most common method for estimating the diffusion parameters $\alpha$ and $D_\alpha$. Recall the definition of the MSD for a drift subtracted particle trajectory, X:

$$MSD_X(n\tau) = \frac{1}{N-n-1}\sum_{j=0}^{N-n} ||X_{n+j} - X_n||^2$$

When a logarithm is applied to the MSD equation(1.6):

$$\log(MSD_X(t)) = \log(2dD_\alpha) + \alpha \cdot \log(t) \tag{2.1}$$

By writing the power law equation in this form, a linear regression can then be fitted with $y_n = \log(MSD_X(t))$ and $x_n = \log(n\tau)$, and the diffusion parameters can thus be estimated using linear least squares:

$$\hat{\alpha} = \frac{\sum_{n=0}^{N}(y_n - \bar{y})(x_n - \bar{x})}{\sum_{n=0}^{N}(x_n - \bar{x})^2},\ \hat{D}_\alpha = \frac{1}{2d}\exp(\bar{y} - \hat{\alpha}\bar{x}) \tag{2.2}$$

where $\hat{\alpha}$ is the regression line slope and $\hat{D}_\alpha$ is the intercept.

LS is easy to implement and cheap to calculate, making it the popular choice when estimating the diffusion parameters, however it can have trouble with accuracy if the MSD is not an exact power law. Experimentally this comes from low and high frequency error. High frequency noise, an effect of camera error, is caused by two things: inaccurately recording the true position of a bead at a given time, and the fact that these beads are in continuous motion but the time series to represent them is discrete. Figure 2.2 shows how high-frequency error can affect the MSD. Until recently, the only way was to account for high-frequency error was by restricting the lag times used to compute LS; discarding those lag times of the MSD most polluted by high frequency noise. This discards the smallest lag times but does not wholly solve the problem as high frequency error is embedded at all lag times and can still cause incorrect parameter estimation, particularly

for low mobility particles. Low frequency noise is caused by the drifting of the particles with respect to the focal plane. This has the effect of raising the MSD at the highest lag times as drift causes an increase in the displacement of beads as time increases, as shown in Figure 2.1. It is common practice to account for drift by computing the MSD from the drift subtracted increments. There are two such ways to do so: subtracting the mean increment, and subtracting the linear regression line; both methods assume the underlying drift is linear and independent in X and Y.

The mean increment method is computed by first calculating the average increment in both X and Y and then subtracting the average from each individual increment: $\Delta X = \Delta X - \overline{\Delta X}$. Subtracting the mean increment from every increment in the particle trajectory then forces the mean of the resulting trajectory to be zero, i.e. it has a global effect of forcing the path to close - initial and terminal position are identical, thus distorting the MSD. This causes the a "waterfall" effect in the MSD at the highest lag times, as evidenced in Figure 2.1.

The regression method first fits a regression line to the X & Y components of the trajectory, $X(t) \sim a \cdot t + b$, where a and b are $1 \times 2$ dimensional matrices. The slope component of the regression line, a, is then subtracted for all the increments $X = X - a \cdot \tau$. One upside of using this method is that it limits the "waterfall" effect of the mean increment method.

From Figure 2.1 it is evident that drift subtraction is needed as well as how effective it can be. In the first panel, without any drift added, both methods accurately follow the empirical MSD across all lag times. The second panel shows the empirical MSD blowing up at large lag times while both methods are extremely similar to the MSD without any drift added. Both panels show the range that each of the drift subtraction method has: they only minimally affect the MSD when there is no drift while accurately bring the MSD down in the presence of large drift. Now comparing the methods themselves, it is evident that both give near identical results at the low and middle lag times while diverging at the highest lag times. Due to the mean increment method causing a waterfall effect where the MSD is pulled down to zero, whenever LS is discussed, the regression method is technique used to subtract drift.

To avoid high-frequency camera error at low lag times as well as low frequency drift at larger lag times, as even with drift subtraction the MSD is still distorted at the highest lag times, the LS regression line is traditionally fit within a time window based on domain knowledge and visual inspection of the empirical MSD to assess where it looks straight, in our case between 0.1 and 1 or 2 seconds. This trimming of the MSD for estimation of the diffusion parameters, $\hat{\alpha}$ and $\hat{D}_\alpha$, only works if the retained MSD window is free of noise.

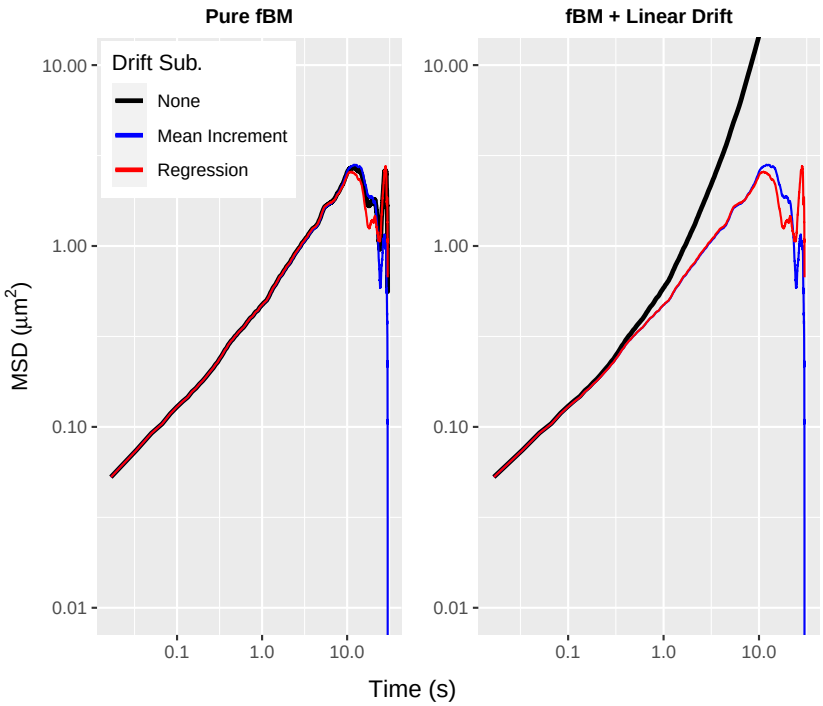


Figure 2.1: Comparing two linear drift subtraction methods on a simulated fractional Brownian motion trajectory. First trajectory has no linear drift added, while the second trajectory has constant linear drift added at each increment.

This can be difficult to assess when the mobility of the particle is close to the noise floor, at which point the particle's movement cannot be separated from the fluctuations of an immobile particle, further discussed in chapter 2.6.

## 2.2 Full Parametric Model

A location-scale model Ling (2021) is used to model the particle trajectory:

$$X(t) = \mu t + \Sigma^{\frac{1}{2}} Z(t) \tag{2.3}$$

Where $\mu = (\mu_1, ..., \mu_d)$ is a d-dimensional vector of linear drift, $\Sigma_{d\times d}$ is a symmetric positive definite scaling matrix, and $Z(t) = (Z_1(t), ..., Z_d(t))$ are independent and identically distributed, iid copies of a continuous stationary increment, CSI, Gaussian process with mean zero and MSD defined as

$$MSD_Z(t) = \eta(t|\varphi)$$

such that the MSD of the drift subtracted process $\tilde{X}(t) = X(t) - \mu t$ is given by

$$MSD_{\tilde{X}}(t) = \frac{1}{d}\,\text{tr}(\Sigma) \cdot \eta(t|\varphi)$$

For the purposes of this research $Z_i(t) = B_\alpha(t)$, that is fractional Brownian motion, in which case the diffusivity coefficient, $D_\alpha$ is determined by

$$D_\alpha = \frac{1}{d} \cdot \text{tr}(\Sigma) \tag{2.4}$$

A fully parameterized model has the benefit of being able to use the MSD for all lag-times while also performing sophisticated denoising to more accurately capture the underlying signal. This is in contrast to LS which is only able to fit to the MSD in a lag-time window in order to minimize the effect of noise, causing the majority of the MSD to be discarded from analysis. In addition, LS does not have any method to account for high-frequency error, while each of the parametric models has had lease one parameter to account for noise, thus allowing for the model to capture the true signal of the bead through the noise while LS can only fit to signal + noise.

As mentioned, a great advantage of using a fully parameterized model as compared to semi-parametric model like least squares is that the model can determine localization errors by distinguishing between the true particle position, $X_n$, and the recorded value, $Y_n$ for any time at time $t = n \cdot \tau$. The following sections will go over two different models for estimating high frequency localization error; the first being the Savin-Doyle error model put forth in Savin (2005) which seeks to have physical parameters to describe the noise and the auto-regressive moving average (ARMA) model as described in Ling (2021) where the noise parameters are non-physical.

### 2.3 Savin-Doyle Error Model

In the Savin and Doyle error model the high-frequency noise is decomposed into two sources: static and dynamic. Static noise is caused by measurement error from the recording of the position of the particle at a given time. Savin and Doyle represent the static error in terms of an additive model with the form:

$$Y_n = X_n + \epsilon_n$$

where $\epsilon_n$ is a d-dimensional stationary process independent of $X(t)$. For a wide range of signal-to-noise ratios, Savin and Doyle report that $\epsilon_n$ is effectively white noise, Savin (2005) which has the effect of raising the MSD at the shortest lag-timess.

While Savin and Doyle define static noise to be from measurement error from the recording and subsequent tracking of the particle trajectory, the dynamic noise is defined as the error caused by the movement of the particle during the camera exposure time, i.e. for each frame a singular position of the particle is recorded however in reality the particle is always in continuous motion. Thus if the camera exposure time, $\tau$ is $\tau < \Delta t$ (as exposure time has to be less than the frame rate) the recorded position of the particle at time $t = n \cdot \Delta t$ is given by:

$$Y_n = \frac{1}{\tau} \int_0^\tau X(n \cdot \Delta t - s) ds$$

Larger values of $\tau$ have the effect of lowering the MSD at the smallest lag-times, as shown in in Figure 2.2. Combining the static and dynamic models, the full Savin-Doyle error model, fSD, is then:

$$Y_n = \frac{1}{\tau} \int_0^\tau X(n \cdot \Delta t - s)\, ds + \epsilon_n \tag{2.5}$$

The fSD model has two significant limitations. Firstly, as Figure 2.2b shows that the Savin-Doyle model can only bend slightly to correct for negatively biased MSDs at the lowest lag times. The model has a greater bend the closer the camera aperture time, $\tau$, is to the frame-rate. However, this is usually not the case in most experimental setups where $\tau$ is typically an order of magnitude smaller than $\Delta$t, which causes the effect of the dynamic error to be very small and oftentimes insufficient to fit to larger negative MSD biases. Secondly, the fSD model has one parameter, $\epsilon_n$, that raises the MSD and another parameter, $\tau$, that lowers it. This can lead to identifiability issues when fitting the model which then affects the estimation of the diffusion parameters. However, as shown in Figure 2.2, the fSD model is more adept than other models at fitting to a larger rise in the MSD at the lowest lag times.

### 2.4 ARMA model

The ARMA model Ling (2021) uses non-physical parameters to model the high-frequency camera error rather than the physical parameters of the fSD model. This is done in an attempt to provide enough flexibility to accommodate a wide range of MSD behavior. This is accomplished by using an autoregressive/moving average ARMA(p,q) type to model the position of the particle, again where $Y_n$ is the recorded position and

$X_n$ is the true position:

$$Y_n = \sum_{i=1}^{p} \theta_i Y_{n-i} + \sum_{j=0}^{q} \rho_j X_{n-j},\ n \geq r = \max(p, q) \tag{2.6}$$

For the initial cases where $0 \leq n < r$, $Y_n$ is then defined via stationary increment process $\Delta\boldsymbol{\mathcal{X}} = \{\Delta X_n, n \in \mathbb{Z}\}$. The increment process $\Delta\boldsymbol{\mathcal{Y}} = \{\Delta Y_n, n \in \mathbb{Z}\}$ defined by

$$\Delta Y_n = \sum_{i=1}^{p} \theta_i \Delta Y_{n-i} + \sum_{j=0}^{q} \rho_j \Delta X_{n-j} \tag{2.7}$$

is a well-defined stationary process which can be causally derived from $\Delta\boldsymbol{\mathcal{X}}$. In addition, setting $Y_n = \sum_{i=0}^{n-1} \Delta Y_i$ obtains the ARMA relation 2.6 for $n \geq r$. It is shown in Ling (2021) that $\mathbf{Y}$ accurately models the high frequency error of $\mathbf{X}$ if and only if

$$\rho_0 = 1 - \sum_{i=1}^{p} \theta_i - \sum_{j=1}^{q} \rho_j \tag{2.8}$$

The fractional moving-average, fMA, noise model is the simplest of the ARMA(p,q) models with $p = 0$ and $q = 1$, from (2.6) and (2.8) the model is given by:

$$Y_n = (1 - \rho)X_n + \rho X_{n-1} \tag{2.9}$$

Figure 2.2a shows the MSD of fMA, for ranges of $\rho \in (-1, \frac{1}{2})$, compared to that of fSD. the fMA model is comparable to the fSD model in its ability to affect the MSD at low lag times. When $\rho > 0$ the MSD is lowered at the lowest lag-times and when $\rho < 0$ the MSD is raised. Both noise models have a similar ability to raise the MSD at the smallest lag times, while the fMA model has a much higher capacity to lower it. This highlights the strength of the ARMA noise model as it able to do this using a single noise parameter while the Savin-Doyle model requires two.

A more flexible two-parameter ARMA model, and the one focused on for the duration of this work, is with p = 1, q = 1, the first order auto-regressive moving average, fARMA, model given by (2.6) and (2.8) is:

$$Y_n = \theta Y_{n-1} + (1 - \theta - \rho)X_n + \rho X_{n-1} \tag{2.10}$$

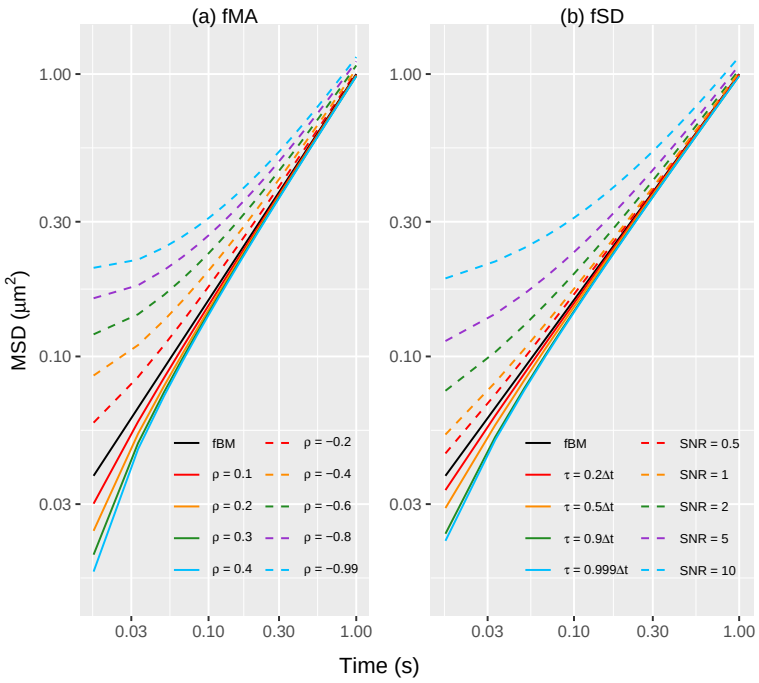


Figure 2.2: (a) MSD of the fMA model for different values of $\rho$. (b) MSD of the fSD model for different values of $\tau$ and SNR.

### 2.5 Parameter Estimation

To estimate the parameters of the fBM location scale model, 2.3, it is convenient to transform to an unconstrained basis; this is done in order to improve model convergence around the parameter endpoints in the standard basis. Since $\alpha \in (0, 2)$ an intuitive unconstrained transformation is:

$$\phi_1 = \text{logit}(\alpha, 0, 2),$$

where the generalized logit transformation is given by:

$$\text{logit}(x, L, U) = \log\left(\frac{z}{1-z}\right), z = \frac{x-L}{U-L} \tag{2.11}$$

Similarly, the noise parameters are transformed using the logit transform (2.11): for the fARMA model $\phi_2 = \text{logit}(\rho, -1, 1)$ and $\phi_3 = \text{logit}(\theta, -1, 1)$. The drift coefficients, $\mu$, are inherently unrestrained, so the last parameter to transform is the scaling matrix $\Sigma$. The unconstrained parametrization for $\Sigma$ is:

$$\lambda = (\log(tr(\Sigma)), \log(\Sigma_{11}/\Sigma_{22}), \text{logit}(\kappa, -1, 1)), \kappa = \frac{\Sigma_{12}}{\sqrt{\Sigma_{11}\Sigma_{22}}}$$

Optimization is then done using maximum likelihood estimation and parameters are converted back to the real basis from the computational basis. For $\phi_1$, $\phi_2$, and $\phi_3$ this is done using the ilogit function:

$$\text{ilogit}(x, L, U) = L + \frac{U - L}{1 + e^{-x}} \tag{2.12}$$

Thus the calculation for the diffusion parameters $(\alpha, D_\alpha)$ is $\alpha = \text{ilogit}(\phi_1, 0, 2)$ and $D_\alpha = \frac{1}{d}\, e^{\lambda_1}$. Only $\lambda_1$ is needed to calculated $D_\alpha$ as Equation 2.4 shows only the trace of the scaling matrix, $\Sigma$ is used which corresponds to the computational parameter $\lambda_1$.

### 2.6 Advances in the classifier for beads entangled in the noise floor

Beads that become embedded in mucosal flakes exhibit low mobility, with $\alpha < 0.3$. At the lowest levels of mobility, $\alpha < 0.1$ fARMA can become unstable in its estimation, most notably in the estimation of the diffusion parameter $D_\alpha$.

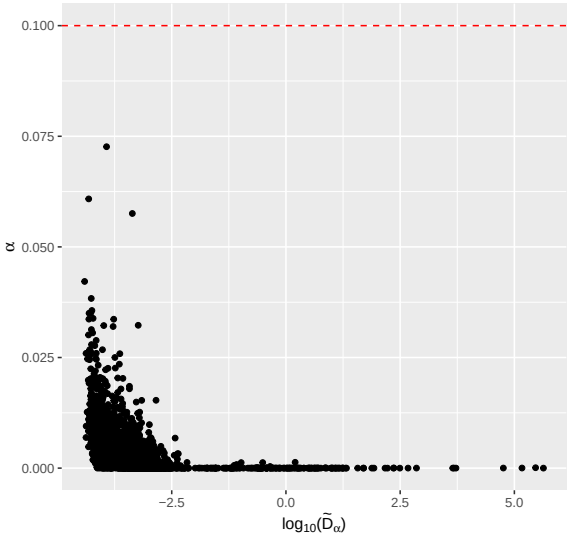


Figure 2.3: Plot of $(\alpha, \tilde{D}_\alpha)$ values for stuck beads, i.e. beads whose signals should only be noise. Notice the broad range of $\tilde{D}_\alpha$ estimates: almost 10 orders of magnitude between them, while the $\alpha$ estimation is relatively consistent. The dashed red line corresponds to the $\alpha$ cutoff we use when determining whether a bead is in the noise floor.

In addition to instability of the estimation of $D_\alpha$, beads with a small estimated $\alpha$ value are likely to be indistinguishable from beads that are physically glued to a stationary plate - they are so entrapped in the mucin flakes that their signal is essentially all noise. Figure 2.3 shows the $(\alpha, \widetilde{D}_\alpha)$ estimates for purely stuck beads whose signal is entirely caused by noise. $\alpha = 0.1$ is thus chosen as the cutoff for beads declared in the noise floor. For such cases, we say that the true signal and the noise are too intertwined for an accurate

estimation of the diffusion parameters and any estimates are recorded as being in the noise floor and then discarded from further analysis.

In certain situations, typically when $\alpha$ is small, i.e. $0.1 < \alpha < 0.3$, there can be slow convergence, or no convergence once the optimization time has elapsed. This happens because the default initial values for the optimization are 0 in the computational basis, corresponding to $\alpha = 1$ in the real basis. This type of situation is of particular interest because such low mobility is common for beads in mucosal flakes.

To improve the chances of successful termination, a predictor-corrector method is used with the MLE models: diffusion parameters, $\alpha$ and $D_\alpha$, are first estimated using LS and then these estimates are used as the initial point for the numerical optimization. All other parameters to be optimized are still initialized at 0 in the computational basis as LS has no capability to estimate them.

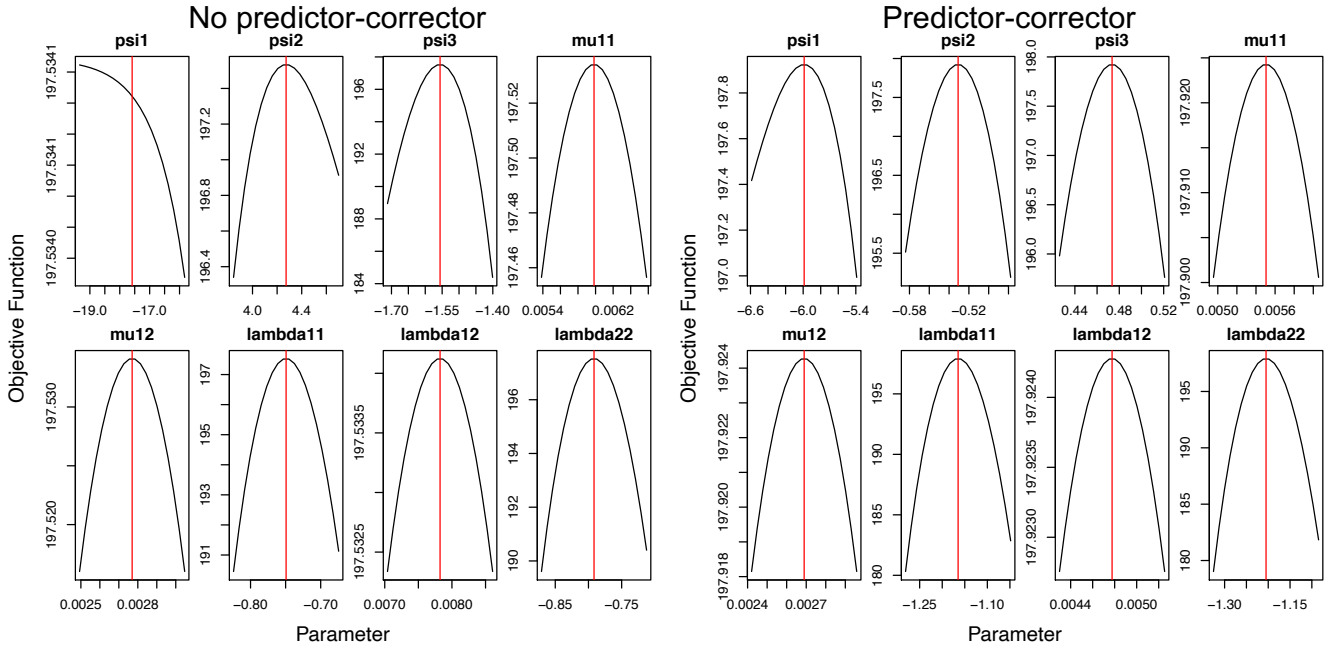


Figure 2.4: Convergence plots on the same trajectory with no initial guess versus initial guess for $\alpha$ supplied from LS. Notice change in estimate for all $\psi$ and $\lambda$ values.

Figure 2.4 shows the improvement in convergence when the LS predictor to fARMA corrector is implemented. Initially $\phi_1$, corresponding to $\alpha$ in the real basis has not converged after the computational time has been reached, but with the predictor-corrector all eight of the parameters converge. This implementation improves the MLE model's ability to converge to an estimation without a significant increase in run-time as LS is a cheap computation. The improvement in convergence to the $\phi_1$ parameter also significantly changes

to the other parameters, notably those corresponding to noise and the scaling matrix.

### 2.7 Parameter Recovery

Now that the fARMAs model has been created and appears to accurately improve upon fARMA in cases of high static noise, as evidenced by Figure 2.8, fARMAs is now tested to see how well it can recover both the diffusion and noise parameters. Parameter recovery is applied to both fARMA and fARMAs, with fARMA acting as a comparison as it is the most similar model to fARMAs. Diffusion and noise parameters are chosen to reflect experimental data at all levels, from water-like signals, to flake-like signals, to entangled in the noise floor.

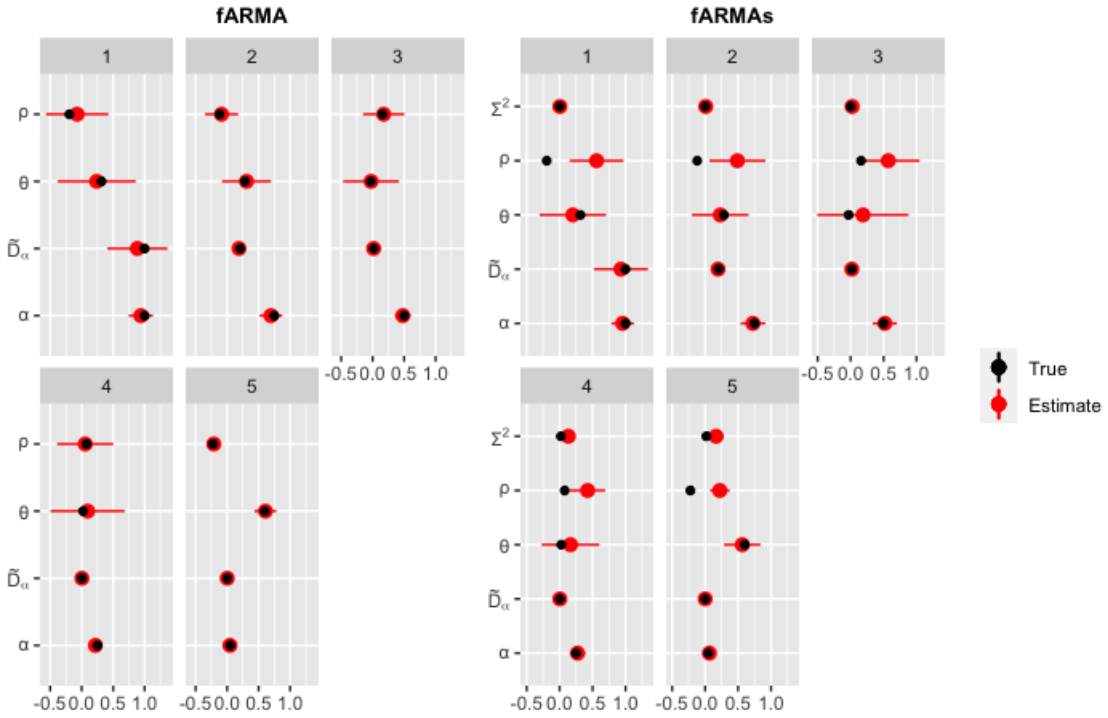


Figure 2.5: Plot of the parameter recovery for noise and diffusion variables for both the fARMA and fARMAs mode. The black dot represents the true value of each parameter, the red dot is the mean over the 100 trajectories with bars representing two times the standard deviation.

fARMA and fARMAs are simulated with the same $\rho$, $\theta$, $\alpha$, and $D_\alpha$ values while fARMAs also has a $\Sigma^2$ parameter that represents white noise. Once a trajectory as been simulated and each of the parameters have been recovered, $D_\alpha$ is then converted to $\widetilde{D}_\alpha$ in order to make comparisons between simulations; the noise parameters and $\alpha$ can already be compared across beads and thus do not need to be transformed. For each set of parameters, 100 trajectories are simulated and the parameters are recovered and then compared to the

true value, as shown in Figure 2.5. The predictor-corrector method is used for both models, with $\alpha$ being initialized using lease squares; all other parameters are still set to be zero in the computational basis.

Figure 2.5 shows how well both the fARMA and fARMAs models are at recovering the parameters used to simulate a particle trajectory. Both models are able to accurately recover the diffusion parameters, relative error less than $10\%$, for trajectories outside of the noise floor. Both models are less accurate at recovering the noise parameters. This is evident from both the difference between mean and true value as well as the larger standard deviation for both the $\theta$ and $\rho$ parameters. One reason why fARMAs is performing worse than fARMA with regards to noise parameter recovery is that both $\theta$ and $\rho$ can raise and lower the MSD, which allows for a better fitting to the empirical MSD and thus recovery of the diffusion parameters (Figure 2.8), $\Sigma^2$, used to calculate $\epsilon$ in Equation 2.13, can only raise the MSD at the lowest time scales (Figure 2.2). Therefore if the dominant high-frequency error is from the static component, fARMAs would be the better model, but when the dynamic component dominates, then fARMA could be the better model. In order to deal with this, *when analyzing experimental datasets, both the fARMA and fARMAs models are used to estimate parameters. For each individual experimental trajectory, the selected model is whichever model MSD is closest to the empirical MSD*.

### 2.8 Comparing LS and fARMA

In order to compare the accuracy of LS and fARMA to each other, a set of synthetic truth sets are used. The values of the diffusion parameters used to generate truth sets were selected in order to sample the range of values that appears in experimental data. The six ($\alpha$,$\tilde{D}_\alpha$) pairs used are: $(0.999, .43)$, $(0.75, 0.108$, $(0.5, 0.0108)$,$(0.25, 0.0027)$, $(0.15, 0.001396)$, and $(0.05, 0.0009587)$.

For each pair two different error models are applied: one with just low frequency drift added and the other which is a combination of the same low frequency drift but high frequency camera error is also added. In order to not bias the results, as simulating and estimating with the same model should return high accuracy, the Savin and Doyle error model, equation 2.5 is used which includes both static and dynamic error. Drift is assumed to be constant and linear.

Of the six ($\alpha$,$\tilde{D}_\alpha$) pairs, one corresponds to pure diffusion, i.e. $\alpha = 1$ and $\tilde{D}_\alpha = 1$, one to a particles in the noise floor, two corresponding to beads embedded in mucosal flakes, and two giving signals between those embedded in flakes and those in a pure water solution, corresponding to beads on the periphery of the flake and more dilute mucin and water mixture. For each combination of ($\alpha$, $\tilde{D}_\alpha$) and error model, 12 in total, one hundred trajectories are simulated using the Savin-Doyle noise model, allowing for physical noise

parameters. The dynamic noise parameter, $\tau$, corresponding to camera exposure time is held constant for each of the $(\alpha,\tilde{D}_\alpha)$ pairs, defining a consistent camera setup for all simulations, while the signal-to-noise ratio lessens as $\alpha$ and $\tilde{D}_\alpha$ both decrease, representing the true signal of the particle becoming more entangled with the noise as it exhibits less mobility. The two diffusion parameters are then estimated, as well as their standard errors, using both LS and fARMA with a predictor-corrector. Standard errors for LS were calculated using the equation from Zhang (2018). It should be noted that when only estimating the diffusion parameters that LS is significantly faster than fARMA, or any of the MLE based models, but when accounting for the standard error calculation LS is in fact slower than fARMA. Figure 2.6 shows the mean estimate as well as error bars corresponding to twice the mean standard error for each.

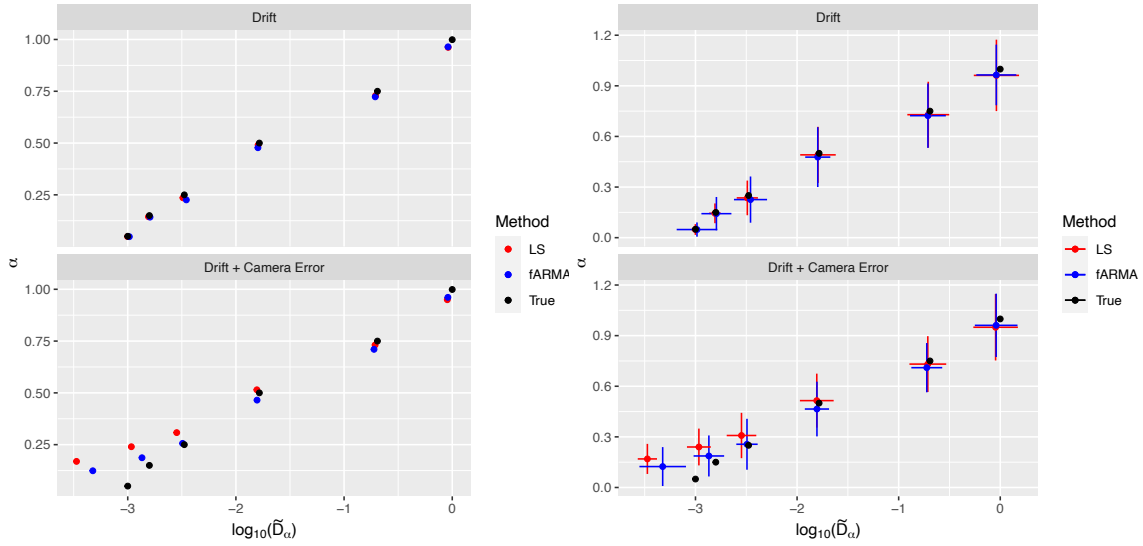


Figure 2.6: $(\alpha, \tilde{D}_\alpha)$ estimates for each of the six bead pairs for the two error models: only low frequency and low and high frequency. The right panel is the same as the left panel but with bars representing two times the standard error in both $\alpha$ and $\tilde{D}_\alpha$.

Figure 2.6 shows that without the presence of high-frequency noise, i.e. the only source of error coming from low-frequency drift, both LS and fARMA are both accurate across all six $(\alpha, \tilde{D}_\alpha)$ pairs. For five of the six pairs the error bars are similar for LS and fARMA, however we see that for the truth set in the noise floor fARMA has a significantly larger error for the $\tilde{D}_\alpha$ estimation than LS. This result should be expected as both methods have similar ways to deal with drift and thus get alike estimates when fitting to the ”pure” signal (once drift has been accounted for).

More can be gleaned in the comparison between LS and fARMA when examining the six truth sets that had both the drift and camera error. Table 2.1 shows the relative errors for the two estimation methods

| Pair | True $(\alpha, D_\alpha)$ | Method | $\alpha$ Error | $\widetilde{D}_\alpha$ Error |
|---|---|---|---|---|
| 1 | $(0.999, .43)$ | LS | 0.049 | 0.099 |
| 1 | $(0.999, .43)$ | fARMA | 0.038 | 0.088 |
| 2 | $(0.75, 0.108)$ | LS | 0.025 | 0.048 |
| 2 | $(0.75, 0.108)$ | fARMA | 0.053 | 0.070 |
| 3 | $(0.5, 0.0108)$ | LS | 0.030 | 0.051 |
| 3 | $(0.5, 0.0108)$ | fARMA | 0.070 | 0.048 |
| 4 | $(0.25, 0.0027)$ | LS | 0.233 | 0.149 |
| 4 | $(0.25, 0.0027)$ | fARMA | 0.025 | 0.036 |
| 5 | $(0.15, 0.001396)$ | LS | 0.600 | 0.318 |
| 5 | $(0.15, 0.001396)$ | fARMA | 0.246 | 0.145 |
| 6 | $(0.05, 0.0009587)$ | LS | 2.385 | 0.664 |
| 6 | $(0.05, 0.0009587)$ | fARMA | 1.479 | 0.524 |

Table 2.1: Table showing the relative error between the mean values of $\alpha$ and $\widetilde{D}_\alpha$ for each set of diffusion parameters estimated using both LS and fARMA. Due to physical relevance, only the errors from the simulations using Savin and Doyle error model are included.

visualized in Figure 2.6. There is little change between the drift and drift plus camera error results for the truth sets with the three largest $(\alpha, \tilde{D}_\alpha)$ pairs, those that correspond to being in pure water and the periphery of the flake. This should not be unexpected, as effect of camera error will be lessened when the mobility of the particle is larger and thus the true signal dominates relative to the noise which allows for LS to get an accurate estimate. However, for the pairs corresponding to beads embedded in flakes there is a drop in accuracy.

Table 2.1 backs up what is seen visually in Figure 2.6. For this table, only those results from the simulations generated using the Savin and Doyle error model are included as real experiments always have both low-frequency drift and high-frequency camera error.

But there is a shift, first in the LS estimates as $(\alpha, \tilde{D}_\alpha)$ decreases. With the $\alpha = 0.25$ truth set, fARMA's estimation of both parameters is still close to the true value while LS's $\alpha$ estimate is starting to be less accurate. This is further extended for the $\alpha = 0.15$ and $\alpha = 0.05$ truth sets, where both LS and fARMA lose accuracy with fARMA being the more accurate of the two. This shows the benefit of using a model that incorporates noise parameters when analyzing flake data.

That last comparison between LS and fARMA is done using the elastic and viscous dynamic moduli, G' and G" respectively, shown in Figure 2.7. This figure shows again that in the absence of high-frequency camera error, not LS and fARMA are able to accurately recover the diffusion parameters as the moduli curves are roughly indistinguishable between the two methods and the true value. This accuracy again carries

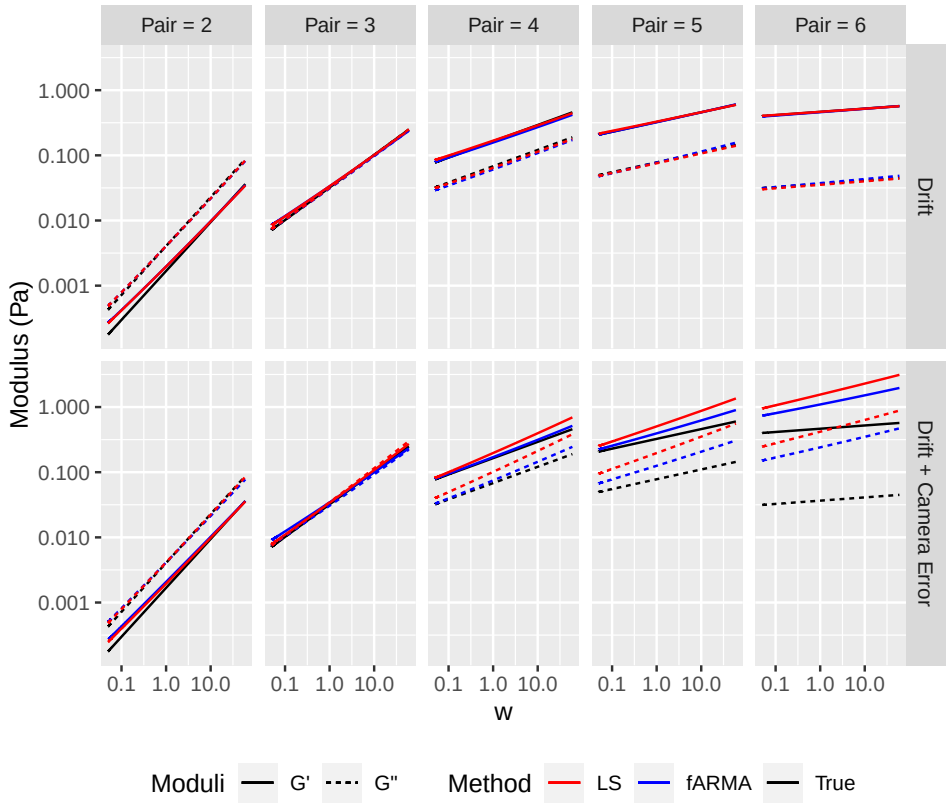


Figure 2.7: The G' and G" moduli curves compared between the true values used to simulate the trajectories and the moduli curves from the average values estimated using LS and fARMAs. Trajectories simulated with and without high-frequency camera error are included.

through for high-mobility trajectories when camera error is added. However the moduli curves begin to break apart starting at the $\alpha = 0.25, D_\alpha = 0.0027$ pair. Here, LS is over-estimating $\alpha$ and underestimating $D_\alpha$ which leads to higher G' & G" values at the smallest frequency which increases as $\omega$ increases, causing the error be greater at the highest frequency values. This is true for fARMA as well but to a lesser degree for both of the "in-flake" pairs.

In the presence of high levels of static noise, the $\epsilon_n$ term in the physical fSD model is larger, both LS and fARMA can fail to accurately estimate both $\alpha$ and $D_\alpha$, as shown in the second plot of Figure 2.8. While both fitted MSDs are able to accurately fit to the empirical MSD, outside of LS severely underestimating the MSD at the lowest lag-times, they are in fact both fitting to the signal + noise instead of only the underlying true signal. This fitting to both the signal and the noise causes both models to over-estimate the value of $D_\alpha$, as shown in the intercepts of Figure 2.8b. *To combat this issue, I created the fARMA + static noise model, fARMAs.* The fARMAs model is defined as the same as the fARMA order 1 model (2.10) but with the

addition of the static noise term from the fSD model. The position of the particle is thus:

$$\begin{aligned} Y_n &= \tilde{X}_n + \epsilon_n \\ \tilde{X}_n &= \theta \tilde{X}_{n-1} + (1 - \theta - \rho) X_n + \rho X_{n-1} \end{aligned} \tag{2.13}$$

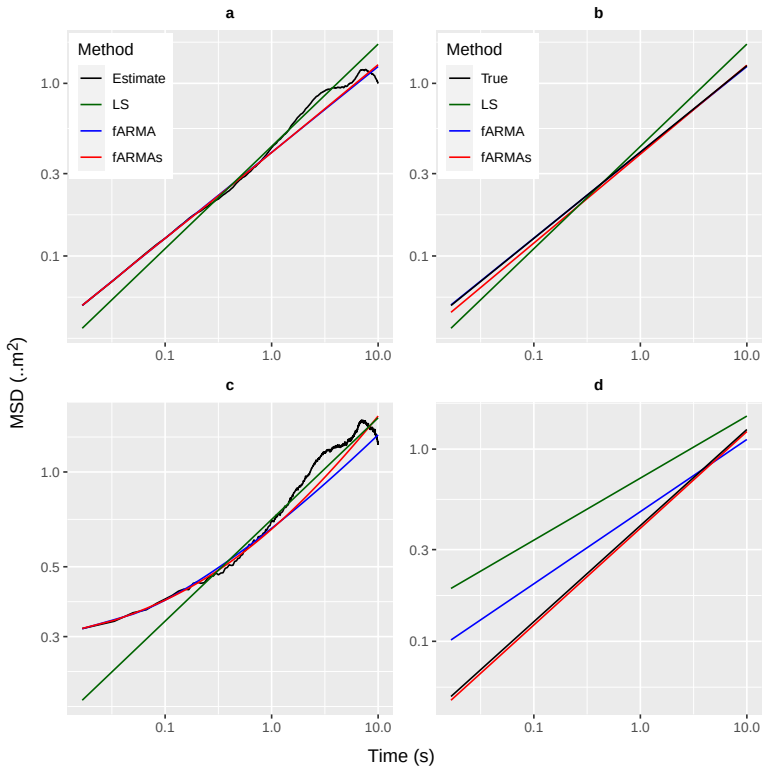


Figure 2.8: (a) plot of a simulated empirical MSD with low noise with three fitted MSDs. (b) The pure fBM MSDs for the three models as well as the true MSD. (c) simulated empirical MSD with high noise with three fitted MSDs: LS, fARMA, and fARMAs. (d) The pure fBM MSDs for the three models as well as the true MSD.Note how all four models visually match up with the high noise empirical MSD, but separate when comparing pure fBM curves.

From Figure 2.8c we can see that both the fARMA and fARMAs models fit reasonably well to the empirical MSD of the simulated trajectory, being able to match the raised values at the highest frequencies, while LS, fit between 0.1 and 2 seconds, does not match up at the highest frequencies but does fit well at the middle and large lag-times. *However this accurate fitting does not necessarily correspond to an accurate estimation of the diffusion parameters*. Figure 2.8d shows that while all three models match up to the MSD of the simulated trajectory, which is determined by the true signal plus high and low frequency error, when compared against pure fBM of the signal, i.e. $MSD_X(t) \sim D_\alpha t^\alpha$, this no longer holds true. *The fARMAs model is able to almost perfectly recover both $\alpha$ and $D_\alpha$*; LS and fARMA both give the approximately the

same estimate of $\alpha$, with fARMA slightly more accurate, and fARMA is more accurate in its estimation of $D_\alpha$ than LS. Plots (a) and (b) of Figure 2.8 show that when there is minimal noise fARMAs is able to fit to the empirical MSD as well as accurately estimate the diffusion parameters. It is evident that all three of the models are accurate when the true signal is less intertwined with noise. *These results demonstrate that fARMAs is able to maintain the accuracy of fARMA for low noise trajectories, i.e. the $\epsilon_n$ term does not dominate with respect to the other noise parameters, but is a necessary improvement for those with a smaller signal-to-noise ratio.*

## 2.9 Comparing LS and fARMA on Experimental Data

When analyzing experimental data, each trajectory can be categorized into three different groups based on the type of high-frequency noise: absence of noise floor, presence of noise floor, reverse(negative) noise floor. Presence of noise floor is distinguished by a flattened raised MSD at the lowest time scale, as shown in Figures 2.2 & 2.9, the reverse noise floor is the opposite of the regular noise floor with the MSD being flattened at the higher lag times, while the absence of noise floor has the standard linear MSD across all lag times. Figure 2.9 shows the fitted MSDs of LS and fARMAs being compared to the empirical MSD for each of the three categories of noise.

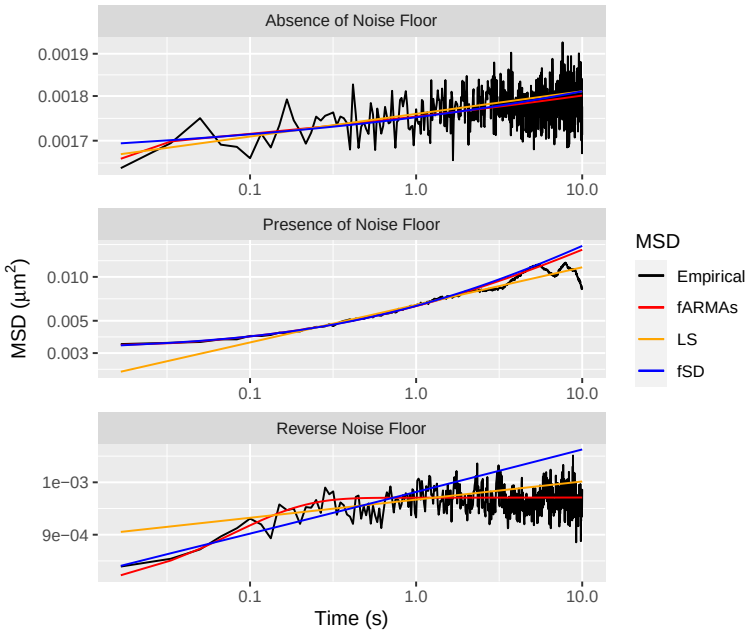


Figure 2.9: (The fitted MSDs of LS and fARMAs compared to the empirical MSD for the three types of noise: standard noise floor, reverse noise floor, and no noise floor.

LS does exactly what it is supposed to - it provides a good fit between $t_{min}$ and $t_{max}$, in this case

$t_{min} = 0.1$ and $t_{max} = 2$, while the rest of the MSD values are discarded. In cases where there is no noise, LS performs well as there is no bending at the highest and lowest lag-times and thus the MSD is linear. However, when in the presence of standard noise or negative noise, LS is unable to bend with the MSD which can cause inaccuracies at extreme lag times. For the reverse noise floor example in Figure 2.9, only part of the bending is contained within $t_{min}$ and $t_{max}$, causing LS to be inaccurate at both the high and low lag-times. In contrast, LS is only incorrect at low lag-times for the noise floor MSD example.

Comparatively, fARMAs is able to handle all three of the types of noise, being able to handle both the raised MSD caused by the noise floor and the lowered MSD from the negative noise floor. Contrasted to the fSD model which fits accurately to the no noise and positive noise MSDs but is incapable of the bending required to fit to the reverse noise floor, being the least accurate of the three models. This further highlights how the non-physical noise parameters of the ARMA model (2.6) have a greater ability to affect the behavior of the MSD and thus are more likely to get an accurate estimation of the diffusion parameters.

CHAPTER 3

# Clustering Methods

## 3.1 Particle Trajectory Classifiers

A natural choice for the classifier of subdiffusive particle trajectories, to compare between particles, is $\theta = (\alpha, \log D_\alpha)$, where use of $\log D_\alpha$ reflects the empirical finding that $D_\alpha$ tends to vary by an order of magnitude within a given experimental setting. I.e., errors in fitting the slope are amplified when one extrapolates to fitting the y-intercept. However, the units of $D_\alpha$ are $\alpha$-dependent, which precludes direct comparisons across beads. There are multiple ways to address this, e.g., one can simply evaluate the MSD at a chosen lagtime $n\tau$, recall the discussion surrounding equation 1.7 above, which gives units of $\mu m^2$ for all beads, and thus admits inter-bead comparisons. A downside of this classifier is that the choice of MSD lag-time $n\tau$ is arbitrary, and one could have chosen any $n\tau$ to evaluate the MSD. Any ng based on these arbitrary choices would have to be tested for robustness of the chosen timescale. We note, however, that if the ensemble data $(\alpha, \log D_\alpha)$ has been estimated by the LS-fARMA method, then it has already used all of the denoised experimental data to produce the denoised classifier $(\alpha, D_\alpha)$ for each bead, which produces a denoised power-law MSD estimate, and therefore the clustering outcome will be relatively robust for all choices MSD $(n\tau)$. This is not the case for standard LS-estimates of $(\alpha, D_\alpha)$, illustrated in Figure 2.8; namely, the LS estimates of MSD has different errors from the true signal MSD at every lag-time $n\tau$! An alternative approach to evaluation of MSD at lag-time $n\tau$ for some n is to non-dimensionalize $D_\alpha$, labeled $\widetilde{D}_\alpha$. Once again, we emphasize that we use the LS-fARMA method on the experimental data to produce the denoised classifier $(\alpha,\ D_\alpha)$ for each bead. Using only experimental scales and a reference fluid relevant to mucus, we define a power law $\alpha$-, spatial dimension d-, and bead radius r-dependent rescaling of $D_\alpha$ normalized with respect to the diffusivity of a bead of the same radius in water,

$$\widetilde{D}_\alpha = \frac{d^{2(\alpha-1)} D_\alpha}{(D_w)^\alpha} \tag{3.1}$$

where $D_w$ is the viscous diffusivity of water for particles of radius r. Note that algebraic manipulations

reveal

$$\widetilde{D}_\alpha = \frac{1}{(4r)^2} \cdot \text{MSD}(t = t_*) \tag{3.2}$$

where $t_* = \frac{(2r)^2}{D_w}$. In other words, $\widetilde{D}_\alpha$ can be interpreted as a multiple of the MSD at a time $t_*$ which depends on the particle radius r, which may not equal an experimental lagtime $n\tau$. For one-micron beads $t_* = 2.33s$ and for 200 nm beads $t_* = 0.018s$. As noted, the clustering algorithm is relatively robust to the lagtime, so any of these choices of MSD give similar clustering results to data that has been denoised by the LS-fARMA method.

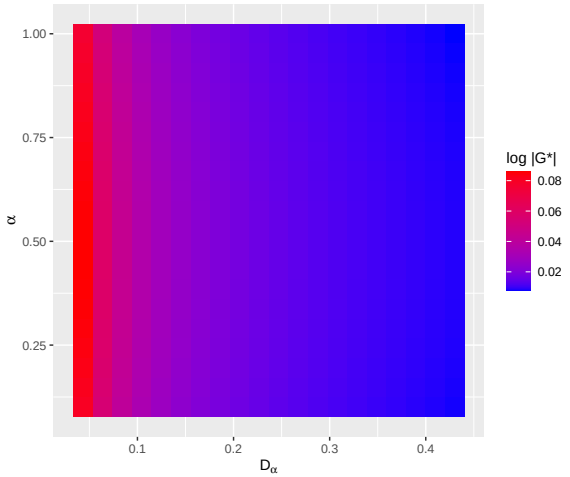


Figure 3.1: Plot of $|G^*(\omega = 1)|$ values over a range of $\alpha$ and $D_\alpha$ pairs. We see that $D_\alpha$ has greater effect over $|G*|$ values than $\alpha$.

Another possible choice of classifier is any of G', G", or $G^*$ for a chosen $\omega$ value. The major strength of using G', G" or $G^*$ as a classifier is that units are consistent, regardless of the $\alpha$ and $D_\alpha$ values as well as comparisons can be made across beads with different radii. Similar to the discussion about the MSD as a classifier, the choice of $\omega$ for any of the moduli functions is again arbitrary. moreover, differentiation between elasticity and viscosity can be difficult without comparison of multiple values, i.e. G' and G" for a given $\omega$ value. An easy workaround to this issue is to use a classifier pair with $\alpha$ and then one of the moduli classifiers. To minimize the influence of $\alpha$ over the second term in the classifier, an intuitive choice for $\omega$ is $\omega = 1$ as the $\omega^\alpha$ term is then one. Furthermore, the $\alpha$ dependence is further reduced by taking the norm of $G^*$, $|G^*| = \frac{k_B T}{\pi r \Gamma(1+\alpha) 6 D_\alpha}$. As Figure 3.1 shows, $|G^*|$ is most affected by $D_\alpha$ with minimal impact from $\alpha$. Therefore $|G^*|$ is a suitable substitute for either $\Delta$ or $\widetilde{D}_\alpha$ as a classifier pair with $\alpha$, as all three have the same

or no units and $|G^*|$ has the added benefit of being able to be compared across different bead sizes. All three particle trajectory classifiers, $(\alpha, \Delta)$, $(\alpha, \widetilde{D}_\alpha)$, and $(\alpha, |G^*|)$ are used in the analysis of beads.

### 3.2 Clustering Analysis

Let $\hat{\theta}_i$ denote the estimate for bead trajectory i of its true classifier value $\theta_i$. A simple choice of classifier is $\theta = (\alpha, \log D_\alpha)$, with an in-depth discussion of various classifiers to follow. Given the classifiers of N trajectories, clustering is performed using the R package **mclust** [Scrucca (2016)] using finite normal mixture models. That is, the classifier estimates $\hat{\theta}_1, ..., \hat{\theta}_N$ are clustered, in the most general case, according to the multivariate normal mixture model

$$J_i \overset{\text{iid}}{\sim} Categorical(\pi_1, ..., \pi_K)$$
$$\theta_i | J_i \overset{\text{iid}}{\sim} Normal(\mu_i, \Sigma_i)$$

where K is the number of clusters and $J_i \in 1, ..., K$ is the cluster to which particle i belongs. **mclust** estimates the posterior membership probability

$$\hat{J}_i = arg\, max_{1 \leq k \leq K} \Pr(J_i = k \,|\, \hat{\boldsymbol{\theta}}_i, \hat{\boldsymbol{\Omega}})$$

where $\hat{\boldsymbol{\Omega}}$ is the maximum likelihood estimate (MLE) of the clustering model parameters $\boldsymbol{\Omega} = (\pi_k, \mu_k, \Sigma_k) : k = 1, ..., K$. **mclust** chooses K by fitting all models with $K \in 1, ..., K_{max}$, and selects the one with the lowest value of the Bayesian information criterion (BIC). It can also impose various constraints on the variance matrices, e.g., proportional variances $\Sigma_k = \tau_k \cdot \Sigma_0$ or diagonal variances $diag(\sigma^2_{k,1}, ..., \sigma^2_{k,K})$ (there are 14 possible variance restrictions in total, see [Scrucca (2016)]).

This is particularly useful when some of the clusters are expected to consist of only a handful of particles, in which case the corresponding unconstrained variance matrices can be very poorly estimated. Once again, **mclust** estimates the posterior membership probabilities $\hat{J}_i, \ i = 1, \ ..., N$ from the best-fitting model (in terms of BIC) among all combinations of cluster sizes K and variance matrix constraints. For the unconstrained variance model, mclust returns identical results when applied to $(\alpha, \log \Delta)$ and$(\alpha, \log \widetilde{D}_\alpha)$, since they are linear combinations of each other. The same is approximately true for $(\alpha, \log |G^*|)$, to the extent that $\Gamma(1 + \alpha) \approx c_1 \alpha^{c_2}$ for $0 < \alpha < 2$. However, clustering results are in principle different for many of the restricted variance functions.

### 3.3 Homogeneity Testing

Now suppose that in addition to $\hat{\theta}_i$, for each trajectory i we have an estimate of the variance of its classifier, $V_i \approx var(\hat{\theta}_i)$. Such a variance estimator is obtained as a direct by-product of the fARMA denoising procedure. In order to test whether the $\hat{\theta}_1, ..., \hat{\theta}_N$ are obtained from a homogeneous cluster, let $\mathbf{Z}_i = \mathbf{V}_i^{-1/2}\hat{\boldsymbol{\theta}}_i$ and $\bar{\mathbf{Z}} = \frac{1}{N}\sum_{i=1}^{N}\mathbf{Z}_i$. Then under the null hypothesis of homogeneity

$$H_0 : \boldsymbol{\theta}_1 = ... = \boldsymbol{\theta}_N$$

The so-called Cochran's Q statistic [Zhang (2018), Cochran (1937), Cochran (1954)]

$$Q = \sum_{i=1}^{N} (Z_i - \bar{Z})'(Z_i - \bar{Z})$$

has a $\chi^2_{p(N-1)}$ distribution under $H_0$, where p is the common number of elements of each $\theta_i$, i.e., in our case we have p = 2. The assumption of homogeneity is then rejected at the $\epsilon$ level when $Q > C_\epsilon$, and $C_\epsilon$ is such that Pr( $\chi^2_{p(N-1)} > C_\epsilon$) $= \epsilon$. Again, we should note that the results of the homogeneity test are identical for $(\alpha, \log \Delta)$ and $(\alpha, \log \widetilde{D}_\alpha)$, and almost identical to those with $(\alpha, \log |G^*|)$, to the extent of that $\Gamma(1+\alpha)$ can be well approximated by a power function of $\alpha$ on the range of $0 < \alpha < 2$. This is due to invariance of the test to linear transformations of the $Z_i$.

CHAPTER 4

# Experimental and Analytical Methods

HBE mucus is reconstituted to match the MUC5B:MUC5AC ratio during three progressive stages of CF, the mixture being a combination of HBE (predominantly MUC5B) plus CaLu3 MUC5AC. The three different combinations of mucin used are: 60% HBE 40% MUC5AC, 80% HBE 20% MUC5AC, and 90% HBE 10% MUC5AC. For all three mucin combinations the weight percent in the solution is constant. Both 1 micron and 200 nm beads are separately implanted into the mucin mixture. These beads are embedded within flakes and then recorded to a video file. These videos are then transcribed into X and Y increments either by hand or via technology. Trajectories are initially recorded in pixels and must converted to measurable units, in this case microns. Every recording setup can have a different pixel to micron conversion ratio, ptm, that must be applied to all coordinate values.

Before any trajectories can be analyzed using any of the methods discussed above, they must first be filtered to ensure all estimated values are accurate. A bead proximity filter is first applied and then a trajectory length filter. The bead proximity filter removes any beads that fall within five diameters of another bead in their initial positions. This filter is necessary as every model previously discussed has the underlying assumption that the beads are undergoing single bead microrheology, i.e. the only forces acting on the beads is from the medium itself, and if any beads are within a sphere of interaction, they could affect the particle's trajectory. Next a simple length filter is applied to ensure that every trajectory analyzed with fARMA and fARMAs is for the full time series. This is done to allow for a more accurate estimation of the diffusion parameters when applying any of the MLE models. This filter only discards a minimal number of beads, as covered in Table 4.1 below. The proximity filter is a per-video filter: each bead is compared to every other in its own video. While the length filter is simply per-bead. It is imperative that the proximity filter is the first one applied to make sure that a bead's potential pair, being within 5 diameters of it, is not discarded prior to proximity filter's use. This is done to insure that a bead pair is not misclassified as an isolated bead.

Beads that appear inside flakes are often in close proximity, within five diameters of one another, an inherent side effect of the flake size relative to the beads. The generalized Stokes-Einstein relation assumes

| Sample | Total Beads | Proximity Filter | Length Filter | Total Left |
|---|---|---|---|---|
| $1\mu m$ HBE + CaLu3 $60\%$ | 154 | 29 | 0 | 125 |
| $1\mu m$ HBE + CaLu3 $80\%$ | 137 | 2 | 0 | 135 |
| $1\mu m$ HBE + CaLu3 $90\%$ | 36 | 11 | 0 | 25 |
| $200nm$ HBE + CaLu3 $60\%$ | 17 | 0 | 0 | 17 |
| $200nm$ HBE + CaLu3 $60\%$ | 31 | 0 | 0 | 31 |
| $200nm$ HBE + CaLu3 $60\%$ | 32 | 0 | 0 | 32 |

Table 4.1: Table showing the total number of beads removed for each of the pre-estimate filters.

the only forces acting on the bead are from the medium itself, while beads in close proximity propagate forces between one another. This coupling of bead fluctuations is the basis for two-bead microrheology (cf. [Mason (1995), Mason (2000), Levine (2000), Crocker (2000), Valentine (2004), Hohenegger (2008)]), which are not analyze here since that data is even more rare than the isolated bead data. Thus, any beads within five diameters are filtered from analysis. The remaining beads, based on the classifier $(\alpha, \tilde{D}_\alpha)$, are then analyzed to first filter all beads indistinguishable from the noise floor (stuck, therefore immobile) for this particular experimental setup. Those that can be distinguished from the noise floor, ranging from just above it to more mobile but not close to mobility in water, are then further analyzed.

Once these filters have been applied, the remaining trajectories have their diffusion parameters estimated using the MLE models. For this research, both fARMA and fARMAs were used: for each bead, both the fARMA and fARMAs models are fit; from there, all of the model parameters are used to construct a fitted MSD curve; the mean squared error, MSE, is calculated with respect to the empirical MSD, and the model with the largest MSE is discarded. fARMA is included as variation of fARMAs where the $\epsilon$ term is held at zero, as it is impossible for the $\epsilon$ parameter to converge to identically zero in the fARMAs model.

After the model has estimated the diffusion parameters, $\alpha$ and $D_\alpha$, there is a final filter applied to the data to remove trajectories that are indistinguishable from the noise floor. The noise floor is quantified by any $\alpha$ below 0.1, as determined by analysis on stuck bead data. Another reason to discard these beads is that for a low $\alpha$ value, there is instability in estimating the pre-factor parameter, $D_\alpha$.

CHAPTER 5

## Results

The fitted MSDs of the fARMAs model are compared to the corresponding empirical MSDs across nine different trajectories. This is done as a first pass to verify with the eye test that the model is accurately fitting to the empirical data. A wide range of mobilities are chosen to cover entire experimental spectrum of pure water to flake, to highly entangled in the noise floor; notice the wide range values on the y-axis of Figure 5.1 to illustrate this point.

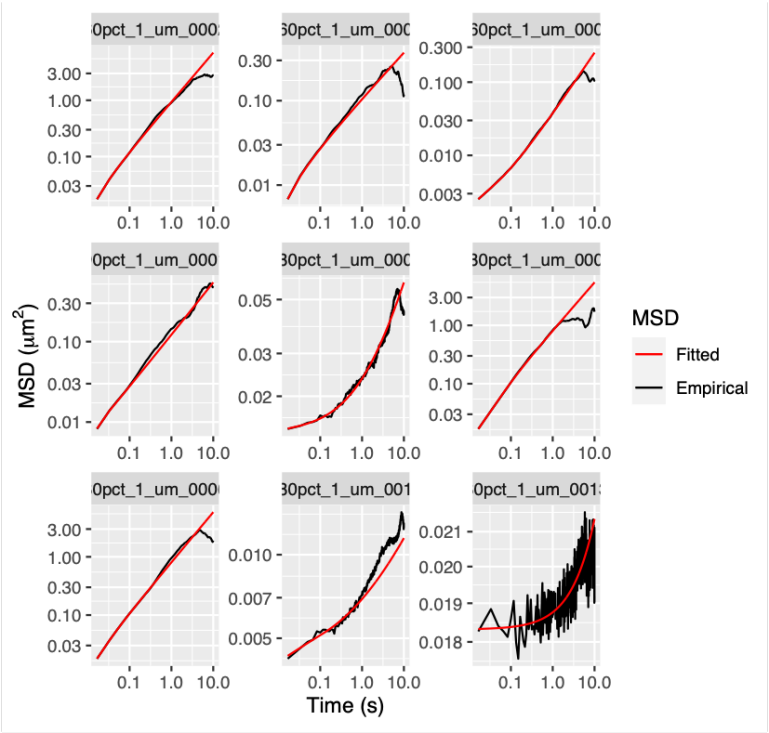


Figure 5.1: Empirical MSDs(black) plotted against fitted MSDs (red) from the fARMAs model for nine different trajectories. Trajectories were chosen so as to sample the entirety of the experimental spectrum of mobility.

As can be seen from Figure 5.1, the fARMAs model does a good job of fitting to the MSD, and thus having an accurate estimation of $\alpha$ and $D_\alpha$. For those trajectories displaying low mobility, with MSD values on the order of $0.01\mu$m there are clear signs of the standard noise raising the MSD at the smallest lag-times.

Here the fARMAs fitted MSD is able to accurately bend with the empirical, further highlighting the point made in Figure 2.9. As expected, all of the MSD corresponding to higher mobility trajectories do not have such signs of noise, as the true signal is orders of magnitude larger than the noise and thus any effects are minimal. There are signs however of the drift subtraction applied, with many of the MSDs having a constant or falling signal at the largest lag-times.

Figure 5.2 gives the $(\alpha, \tilde{D}_\alpha)$ estimates for 1 micron and 200 nm diameter beads in HBE mucus samples from three different treatments of the same HBE sample: HBE + CaLu3 60, 80 and 90 as described in the chapter 4. All datasets support a tri-modal distribution: one cluster reflects a water-like signal; a second cluster is indistinguishable from and buried in the noise floor; and, a third cluster separated from both the water-like and noise floor data, which we call flake-like. The flake-like data exhibits sub-diffusive behavior of beads either within or at the periphery of flakes or in a sufficiently concentrated mucin environment.

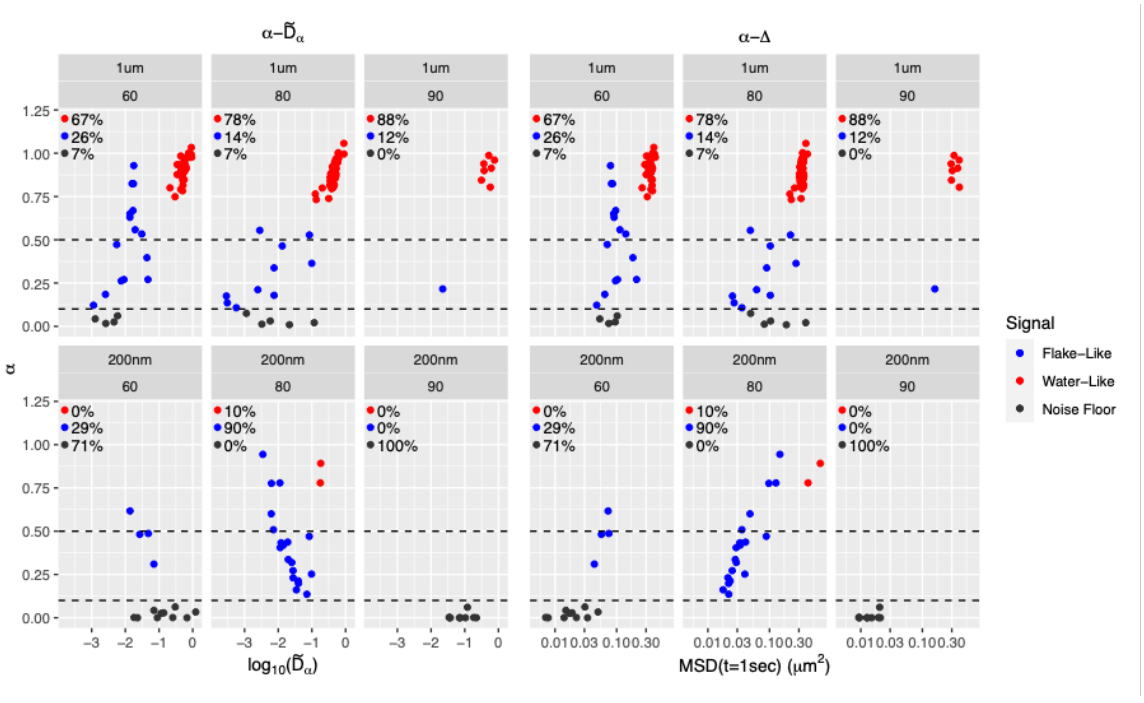


Figure 5.2: $(\alpha, \widetilde{D}_\alpha)$ and $(\alpha, \Delta)$ classifier data for individual, one micron (top) and 200 nm (bottom) diameter beads in three different mucin mixtures. Classifier data is clustered into: water-like (red), flake-like (blue), and noise floor (black) signals.

We draw further consequences from the comparison of 1 micron and 200 nm diameter probes in all three samples.

1. 70% of 1 micron diameter beads exhibit water-like signals versus 4% of 200 nm diameter beads

(0/47 in the 60 and 90 samples and 3/25 in the 80 sample). These statistics of entry into flakes far outweigh the 5:1 expected flake encounter frequency of 200 nm vs. 1 micron diameter beads, supporting several flake structure properties: (i) flake encounters of 200 nm beads almost always lead to entry, implying a high percentage of pores at the boundary of flakes is above 200 nm; (ii) flake encounters of 1 micron beads have a high ( 70%) failure rate of entry, even though each freely diffusing bead likely has many flake encounters, suggesting at most 30% of boundary pores of flakes are 1 micron or larger, and at least 70% of boundary pores are at or below 1 micron. Together, these datasets are consistent with heterogeneous pores at flake boundaries with  70% between 200 nm and 1 micron and  30% above 1 micron.

2. The total within-flake data gives further insights into internal flake pore morphology. The 200 nm data across the three different samples suggests a non-monotone pore structure transition from the 60 to 80 to 90 samples: in the 60 sample, 11/17 beads enter flakes and become sterically trapped, with SNR buried in the noise floor; in the 80 sample, only 1/25 beads enter a flake and become sterically trapped (i.e., with SNR in the noise floor); in the 90 sample, all 30 beads enter and become sterically trapped in pores comparable to their size so that they are indistinguishable from being immobile. We have no insights into how to explain this behavior, but below in Figure 5.2 we see a similar non-monotonicity in rheology.

3. The 1-micron bead data for 60, 80 samples are consistent with a broad pore size distribution so that beads randomly sample outside and within flakes, with some within-flake beads in pores larger than 1 micron and others entering and being trapped in pores slightly larger than a micron, the latter reflected by beads in the noise floor. The 1 micron, 90 sample dataset is smaller, yet suggestive that the pore-size distribution is broader with many multi-micron pores, so that beads freely enter and escape flakes. This would be consistent with a less dense flake formation at the smallest, 10%, CaLu3 MUC5AC consistent with early CF progression.

The top panel of Figure 5.3 presents clustering results with each of the $(\alpha, \log \Delta)$, $(\alpha, \log \widetilde{D}_\alpha)$, and $(\alpha, \log |G^*|)$ classifiers for which the maximum number of clusters is set to $K_{max} = 2$. The classifiers are all in general agreement in distinguishing the water-like beads in the top right corner from the flake-like beads in the bottom left for the experiments with $1\mu m$ beads at $60\%$ and $80\%$ concentration. There are, however, a few particles in the top right corner that are flagged as flake-like, e.g., at $80\%$ with the $(\alpha, \log \Delta)$ and $(\alpha,\ \log \widetilde{D}_\alpha)$ classifiers. This is because mclust requires each cluster to have an elliptical shape. The misclassified points in the top-right corner are very far from the otherwise small elliptical shape of the bulk, and thus get grouped with the flake-like beads, for which the elliptical cluster shape is much larger.

The experiments at $1\mu m$ diameter with $90\%$ concentration and those at 200nm with $60\%$ concentration

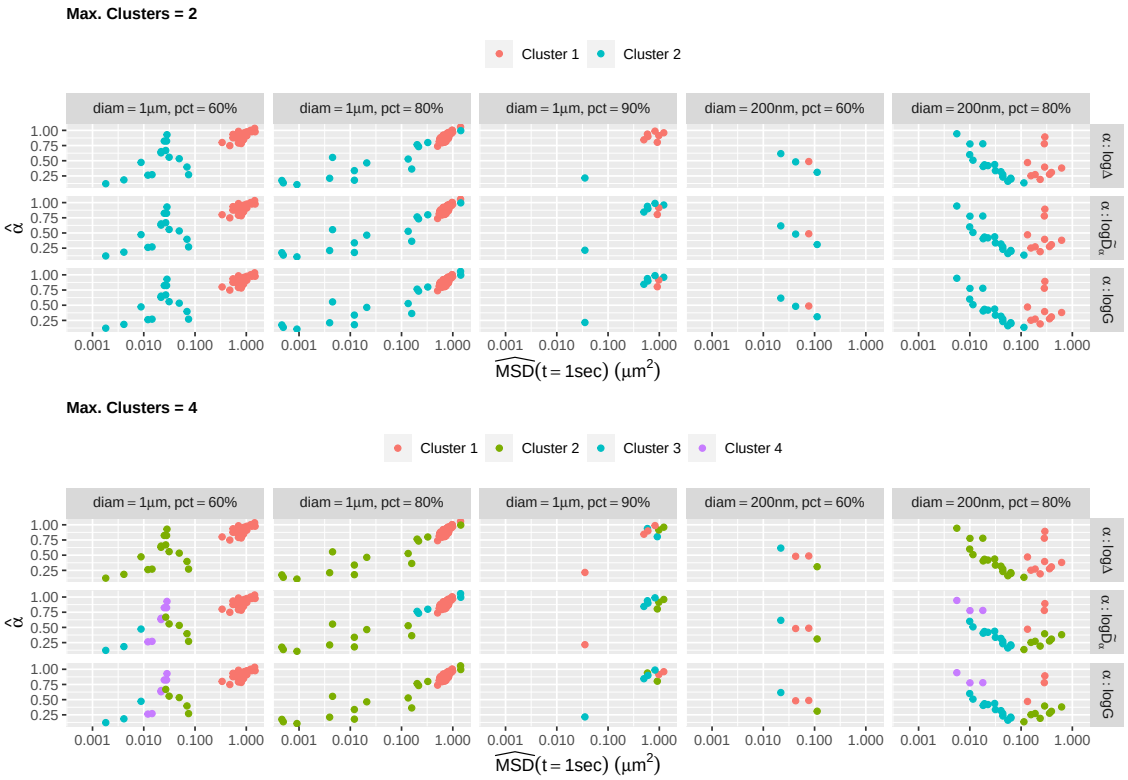


Figure 5.3: Clustering results for classifiers: $(\alpha,\ log\Delta)$, $(\alpha,\ log\widetilde{D}_\alpha)$, and $(\alpha, \log|G^*|)$. The five samples with data above the noise floor are classified into clusters using mclust, where the maximum number of clusters is first set to two, and then to four. While the samples are clustered using each of the specific classifiers, for a one-to-one comparison they are plotted using the same units on the x-axis.

contain too few beads above the noise floor to draw any meaningful conclusions. At 200nm diameter and 80% concentration, all classifiers divide the beads roughly along the vertical line at $\hat{\Delta} = 0.02\mu m^2$. Neither method singles out the two clearly water-like beads in the top-right corner; this is the downside of the elliptical cluster restriction imposed by **mclust**. An alternative might be to define a sub-rectangle in the top right corner of the classifier range that confidently corresponds to pure signals from 200 nm, respectively 1 micron, diameter beads in very dilute mucin solutions. Then all beads outside this water-like corner would be subject to additional clustering and homogeneity tests.

The bottom panel of Figure 5.3 presents results for which the maximum number of clusters is set to $K_{max} = 4$, the hope being that the additional clusters will serve to capture the beads outside the two main elliptical clusters of flake-like and water-like beads. This is the case to some extent, notably for the $1\mu m$ beads at 80% concentration with the $(\alpha, \log\widetilde{D}_\alpha)$ classifier, and for most of the classifiers on 200nm beads at 80% concentration.

Overall, the various classifiers are once again in rough agreement with each other. Two notable exceptions are the $(\alpha,\ log\widetilde{D}_\alpha)$ classifier for $1\mu m$ at $60\%$ concentration, and the $(\alpha, \log \Delta)$ classifier for 200nm at $80\%$ concentration: the former divides the flake-like cluster into three groups whereas the other classifier keeps it as one, and the latter divides the beads into two clusters whereas the other divides them into a consistent set of four. However, a closer inspection reveals in the first scenario that the difference in BIC between the four clusters selected by **mclust** and the two clusters which would have been consistent with all the other classifiers is just under 2.5 units – a difference generally considered to be "barely worth mentioning" [Kass (1995)]. In other words, a slight shift/addition/removal of one or two particles could have easily made **mclust** choose four clusters in this setting as it did for the other classifiers.

The full Bayesian Information Criterion, BIC, results for all clusters are displayed in Figure 5.4, revealing that the same reasoning applies to the second scenario. In other words, mclust could have easily chosen four clusters instead of two.

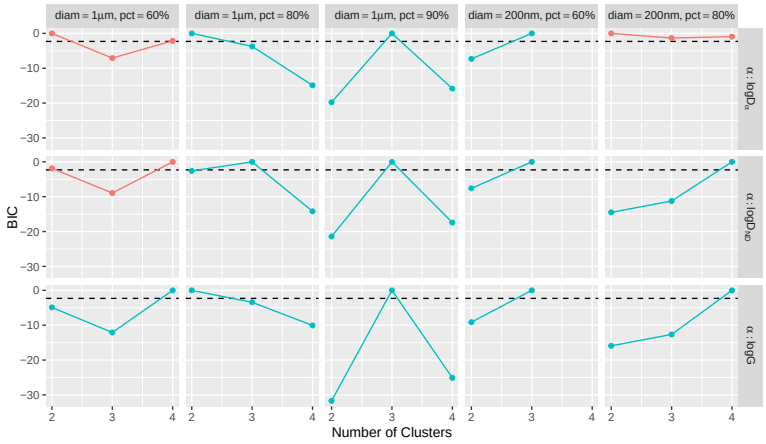


Figure 5.4: BIC for various two-dimensional classifiers. Plotted in red are those for which the difference between the highest and second highest BIC is negligible, i.e., both are above the dashed horizontal line.

Therefore, all classifiers essentially group the 200nm $80\%$ concentration beads into four distinct clusters, two of which have at least half a dozen beads (leftmost and bottom clusters). The classifiers include a bead from the bottom cluster relatively far from the top-right corner. Again, we surmise this is due to **mclust** penalizing heavily against the non-elliptical cluster which would result from grouping the misclassified bead with the rest in the bottom group.

While the five classifiers considered generally agree, none clearly emerges as most consistent with our visual classification into water-like and flake-like clusters. We surmise that the optimal classifier is

experiment-specific, with a much larger number of beads needed to determine which it is. That being said, taking all of the visual and algorithmic clustering results into account, we select a single clustering per experiment from the two panels of Figure 5.3 summarized in Table 5.1.

| Diameter | HBE (%) | $K_{\max}$ | K | Classifier |
|---|---|---|---|---|
| $1\mu m$ | 60 | 4 | 2 | $\alpha : \log \Delta$ |
| $1\mu m$ | 80 | 4 | 3 | $\alpha : \ log\widetilde{D}_\alpha$ |
| $1\mu m$ | 90 | 2 | 2 | $\alpha : \log \Delta$ |
| $200nm$ | 60 | 4 | 3 | $\alpha : \log \Delta$ |
| $200nm$ | 80 | 4 | 4 | $\alpha : \log \widetilde{D}_\alpha$ |

Table 5.1: Selected cluster assignment based on visual clustering and the algorithmic clustering results of Figure 5.3. $K_{max}$ refers to the max number of clusters and K refers to the optimal number of clusters.

In order to assess within-cluster homogeneity, Table 5.2 presents the results of Cochran's Q test applied to each of the clusters of each experiment described in Table 5.1.

| Diameter | HBE (%) | K | Group | Num. Beads | $Q$ | P-value |
|---|---|---|---|---|---|---|
| $1\mu m$ | 60 | 2 | 1 | 38 | 676.3 | 4.6e-98 |
| | | 2 | 2 | 15 | 2771.5 | 0.0e+00 |
| | 80 | 3 | 1 | 49 | 172.9 | 2.5e-06 |
| | | 3 | 2 | 10 | 2372.4 | 0.0e+00 |
| | | 3 | 3 | 5 | 358.6 | 1.3e-72 |
| | 90 | 2 | 1 | 1 | - | - |
| | | 2 | 2 | 7 | 144.7 | 6.7e-25 |
| $200nm$ | 60 | 3 | 1 | 2 | 24.9 | 3.9e-06 |
| | | 3 | 2 | 1 | - | - |
| | | 3 | 3 | 1 | - | - |
| | 80 | 4 | 1 | 3 | 49.2 | 5.3e-10 |
| | | 4 | 2 | 13 | 1023.7 | 8.2e-201 |
| | | 4 | 3 | 8 | 158.7 | 1.3e-26 |
| | | 4 | 4 | 3 | 116.5 | 3.0e-24 |

Table 5.2: Cochran's homogeneity test results for the clusters reported in Table 5.1

All of the resulting p-values are extremely small, indicating that *Cochran's Q test overwhelmingly indicates that the clusters are not homogeneous*. This observed lack of homogeneity is expected for the flake-like clusters as these clusters represent beads that were in different flakes and experiencing different pore structures within each flake, and the phase separation process of flake formation is inherently stochastic. *Furthermore, none of the water-like clusters pass a homogeneity test*. This too is not surprising: the dilution process outside flakes is as stochastic as the flake formation; beads outsides of flakes are in dilute phases

that vary with relative proximity to nearby flakes and degree of dilution, with signals ranging from a pure water-like signal to low mucin concentrations.

*This determination of heterogeneity, both between and within the coarse within-flake and outside-flake bead signals, strongly favors the following data-analysis protocol*: (1) for each of the 3 MUC5B:MUC5AC reconstituted batch samples, and separately for sub-samples with 200 nm and 1 micron beads, use the coarse clustering results to identify beads within and outside of flakes; (2) because nearly all clusters with more than one bead fail the homogeneity test, apply the GSER with the denoised MSD for each single bead; (3) then average the dynamic moduli within each cluster.

These steps yield the within-flake and outside-flake dynamic moduli as revealed by 200 nm and 1 micron diameter probes, for each of the 3 reconstituted HBE samples. For comparison, we also show results using the two alternative applications of the GSER, always applying the methods post clustering, namely averaging within-cluster MSDs and then applying GSER, and averaging within-cluster classifiers and then applying GSER. As shown in the synthetic datasets above, the latter two methods yield equivalent results for normal clusters, and likewise agree with within-cluster averaging in moduli space. These equivalences will not persist even within clusters for the experimental data.

While the clustering results displayed in Figure 5.3 are generally effective at discerning between the water-like and flake-like signal, there are limitations when attempting to determine clusters for those beads with a flake-like signal. This is most apparent in the $(\alpha, \log \Delta)$ classifier, as when $K_{max} = 4$ all of the experiments with "significant" flake-like samples, i.e. $1\mu m$ beads at $60\%$ and $80\%$ concentrations and 200 nm beads at $80\%$ concentration, have the same clusters as with $K_{max} = 2$. However the $(\alpha,\ log\widetilde{D}_\alpha)$ breaks up the flake-like beads into separate clusters for two out of thee three high yield flake samples. Thus, **mclust** is then only applied to the beads with a flake-like signal to further examine potential clusters.

Similarly to Figure 5.3 the top panel of Figure 5.5 presents results for which the maximum number of clusters is set to $K_{max} = 2$. For this $K_{max}$ value, both the $(\alpha, \log \Delta)$ and $(\alpha, \log \widetilde{D}_\alpha)$ classifiers return the same clusters. The classifiers are all in general agreement in distinguishing clusters within beads giving a flake-like signal. The results for the $1\mu m$ beads at $60\%$ concentration and 200nm beads at $80\%$ concentration may seem unexpected, but it is an effect the fact that **mclust** requires each cluster to have an elliptical shape. For both of these samples, **mclust** identifies one population within a small elliptical cluster and thus all other beads are grouped into the second.

The experiments at $1\mu m$ diameter with $90\%$ concentration and those at 200nm with $60\%$ concentration

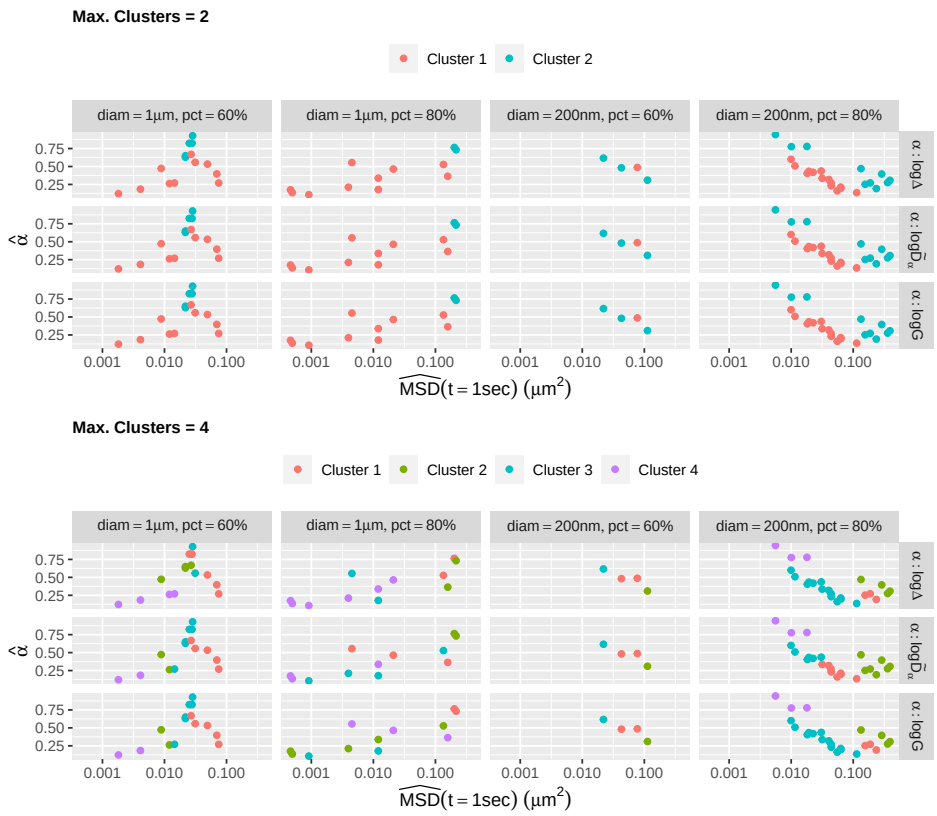


Figure 5.5: Clustering results for classifiers: $(\alpha,\ log\Delta)$, $(\alpha,\ log\widetilde{D}_\alpha)$, and $(\alpha, \log|G^*|)$ for beads giving a flake-like signal. The four samples with data above the noise floor, and more than one bead, are classified into clusters using mclust, where the maximum number of clusters is first set to two, and then to four. While the samples are clustered using each of the specific classifiers, for a one-to-one comparison they are plotted using the same units on the x-axis.

contain too few beads above the noise floor to draw any meaningful conclusions. In fact, the experiment at $1\mu m$ diameter with $90\%$ concentration only have one bead and is thus discarded from this analysis.

The bottom panel of Figure 5.5 presents results for which the maximum number of clusters is set to $K_{max} = 4$, the idea being that there are more than one or two different signals for flake-like beads. This appears to be the case as for the samples outside of the 200nm beads at $60\%$ concentration all four clusters are used.

Overall, the two classifiers are once again in rough agreement with each other. Two notable exceptions are the $1\mu m$ at $60\%$ and $80\%$ concentrations; both occur when grouping beads with middle values of each classifier.

For the $80\%$ concentration, both classifiers agree that there distinct higher and lower mobility clusters but fitting the data into two different clusters in between. There are no consensus clusters for the $60\%$

concentration  certain beads are grouped into the same cluster but no cluster across both classifiers has the same beads in it. The 60% concentration sample is also the only sample where the primary cluster, i.e., the one with the tightest elliptical fit, is not conserved.

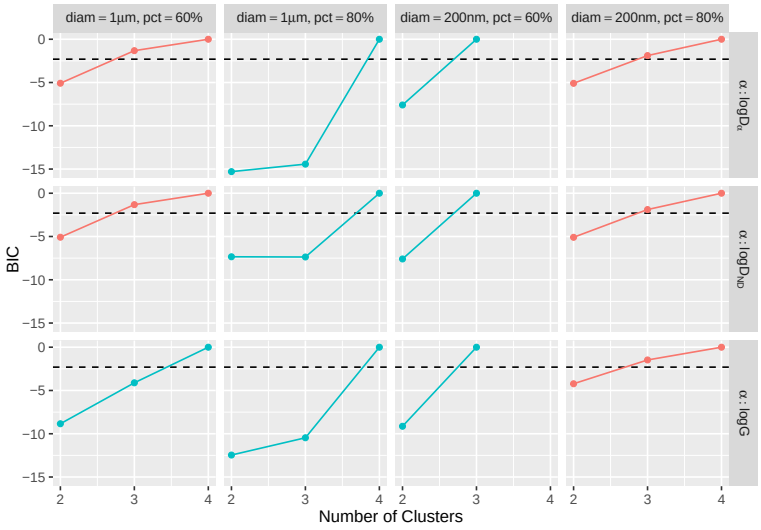


Figure 5.6: BIC for various two-dimensional classifiers on beads giving a flake-like signal. Plotted in red are those for which the difference between the highest and second highest BIC is negligible, i.e., both are above the dashed horizontal line.

The full Bayesian Information Criterion, BIC, results for all clusters are displayed in Figure 5.5. While the classifiers considered generally agree, none clearly emerges as most consistent with a visual classification. We surmise that the optimal classifier is experiment-specific, with a much larger number of beads needed to determine which it is. That being said, taking all of the visual and algorithmic clustering results into account, we select a single clustering per experiment from the two panels of Figure 5.5 summarized in Table 5.3.

As in Table 5.1 the selected single clustering for in-flake beads represented in Figure 5.5 are summarized in Table 5.3

| Diameter | HBE (%) | $K_{\max}$ | K | Classifier |
|---|---|---|---|---|
| $1\mu m$ | 60 | 2 | 2 | $\alpha : \log \Delta$ |
| $1\mu m$ | 80 | 4 | 4 | $\alpha : \log \Delta$ |
| $200nm$ | 60 | 2 | 2 | $\alpha : \log \Delta$ |
| $200nm$ | 80 | 4 | 4 | $\alpha : \log \Delta$ |

Table 5.3: Selected cluster assignment based on visual clustering and the algorithmic clustering results of Figure 5.5. $K_{max}$ refers to the max number of clusters and K refers to the optimal number of clusters

It should be noted that while $(\alpha,\ \log \Delta)$ is the chosen classifier for each of the five samples, for 4 out of

the five samples the $(\alpha,\ \log \widetilde{D}_\alpha)$ classifier returns the same clusters.

| Diameter | HBE (%) | K | Group | Num. Beads | $Q$ | P-value |
|---|---|---|---|---|---|---|
| $1\mu m$ | 60 | 2 | 1 | 38 | 676.3 | 4.6e-98 |
| | | 2 | 2 | 15 | 2771.5 | 0.0e+00 |
| | | Water | Water | 15 | 2771.5 | 0.0e+00 |
| | 80 | 4 | 1 | 49 | 172.9 | 2.5e-06 |
| | | 4 | 2 | 10 | 2372.4 | 0.0e+00 |
| | | 4 | 3 | 5 | 358.6 | 1.3e-72 |
| | | 4 | 4 | 5 | 358.6 | 1.3e-72 |
| | | Water | Water | 10 | 2372.4 | 0.0e+00 |
| | 90 | 2 | 1 | 1 | - | - |
| | | Water | Water | 7 | 144.7 | 6.7e-25 |
| $200nm$ | 60 | 3 | 1 | 2 | 24.9 | 3.9e-06 |
| | | 3 | 2 | 1 | - | - |
| | | 3 | 3 | 1 | - | - |
| | 80 | 4 | 1 | 3 | 49.2 | 5.3e-10 |
| | | 4 | 2 | 13 | 1023.7 | 8.2e-201 |
| | | 4 | 3 | 8 | 158.7 | 1.3e-26 |
| | | 4 | 4 | 3 | 116.5 | 3.0e-24 |
| | | Water | Water | 3 | 116.5 | 3.0e-24 |

Table 5.4: Cochran's homogeneity test results for the clusters reported in Table 5.3

As Table 5.2 shows, the flake-like cluster for each experiment is not homogeneous. This result should not be unexpected as these clusters are an amalgamation of many different flakes whose underlying structures will differ from one flake to the next. One question to answer is whether the beads embedded in an individual flake have any sort of underlying homogeneity, i.e. is there inter-flake heterogeneity but intra-flake homogeneity . To determine this, again only the flake-like signal beads are filtered out from the those with a water-like signal and in the noise floor. A first "test" to quantify potential homogeneity is simply a visual comparison. Figure 5.7 shows all of the beads color coded by which movie in the experiment they appear.

Much analysis is difficult as most samples only have $\sim$2 videos with more than one or two beads in them. However we see generally that beads within flakes clustered together with respect to other beads in the sample. This is most notable in the 1 $\mu$m 60% with the pink, blue, and green videos having a defined distribution. While in the 1 $\mu$m 80% sample, the yellow and blue videos are consistent in one variable, $\alpha$ and $\tilde{D}_\alpha$ respectively, while purple has a core cluster but then a few outliers. The 200 nm 80% sample is the last one with more than one cluster. Here we see the gray and pink video being a bit spread, but having a general cluster shape.

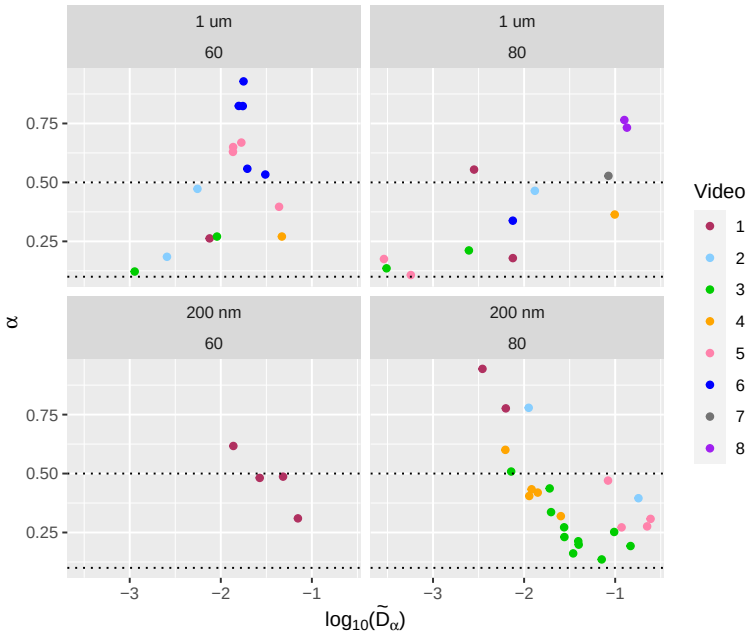


Figure 5.7: $(\alpha, \tilde{D}_\alpha)$ estimates for all of the flake-like beads from Figure 5.2. Then per sample, each video is assigned a unique color.

| Diameter | HBE (%) | Video | Num. Beads | $Q$ | P-value |
|---|---|---|---|---|---|
| $1\mu$m | 60 | 1 | 2 | 65.6 | 5.7e-15 |
| | | 2 | 2 | 441.0 | 1.7e-96 |
| | | 3 | 4 | 124.7 | 1.7e-24 |
| | | 4 | 5 | 102.8 | 1.1e-18 |
| | 80 | 1 | 2 | 6.1 | 4.7e-02 |
| | | 2 | 2 | 30.2 | 2.8e-07 |
| | | 3 | 2 | 4.2 | 1.2e-01 |
| | | 4 | 2 | 0.1 | 9.3e-01 |
| 200nm | 60 | 1 | 4 | 279.4 | 2.1e-57 |
| | 80 | 1 | 2 | 94.1 | 3.6e-21 |
| | | 2 | 2 | 774.7 | 5.9e-169 |
| | | 3 | 11 | 2550.0 | 0.0e+00 |
| | | 4 | 5 | 1222.6 | 1.3e-258 |
| | | 5 | 4 | 182.8 | 8.5e-37 |

Table 5.5: Cochran's homogeneity test results for the clusters shown in Figure 5.7. Any movie that has only one in-flake bead was discarded for better readability.

As Table 5.5 shows, most of the individual videos, i.e. individual flakes, the p-values indicate that the clusters are not homogeneous. Only a few of them have a p-value above the standard $p = 0.05$ threshold; and those that do, or are very close, only have two beads in them. Any individual flake that had at least four beads

embedded in it, still a small sample size, returned an extremely small Cochran Q test value. The results in Tables 5.2 and 5.5 show that there is only minimal evidence for both inter- and intra-flake homogeneity, with the majority of the data pointing to a lack of homogeneity with very small Cochran Q test values.

### 5.1 A scalar metric for power-law viscoelastic fluids: the loss tangent

A fundamental property of viscoelastic media is that, instead of a scalar metric (viscosity for purely viscous, elasticity for purely solid, materials) the viscous and elastic moduli are functions of frequency. So it is appealing to ask if there is a reasonable and informative simpler metric for viscoelastic materials. A standard coarse metric is the loss tangent: $\tan(\delta(\omega)) = G'(\omega)/G"(\omega)$, in general frequency-dependent. When $\delta > \pi/4 : \tan(\delta) > 1$ and the material is sol-like (i.e., loss or viscosity dominated), whereas when $\delta < \pi/4 : \tan(\delta) < 1$, and the material is gel-like (i.e., storage or elasticity dominated).

*For pure power-law viscoelastic materials,* $\tan(\delta)$ *collapses to a scalar function of the MSD power law exponent* $\alpha$*, independent of both frequency* $\omega$ *and the MSD pre-factor* $D_\alpha$. From the GSER equation 1.2 and the power-law moduli formulae 1.9,

$$\tan(\delta) = \frac{G"(\omega)}{G'(\omega)} = \tan\left(\frac{\pi\alpha}{2}\right) \tag{5.1}$$

Thus, gel-like phases correspond to $0 < \alpha < 0.5$ and sol-like phases correspond to $.5 < \alpha \leq 1$. For improved graphical visibility, we plot $\log_{10}(\tan(\delta))$, shifting the gel/sol cutoff from 1 to 0 in log space, so that positive values of $\log_{10}(\tan(\delta))$ correlated to a sol-like phase while negative values correlate to gel-like phase. All water-like data should be sol-like, as all data is above the $\alpha = 0.5$ line in Figure 5.2, all noise-floor data is gel-like, by the choice of $\alpha = 0.1$ to be the noise floor cut off, while all flake-like data lies between these extremes. We are interested especially in the percentage of sol-like and gel-like signals in flake-like data as a coarse scalar metric of heterogeneity.

Figure 5.8 gives a visual equivalent of looking at the $\alpha = 0.5$ cutoff in Figure 5.2 as the separation between sol-like (above the cutoff) and gel-like (below the cutoff) local sample properties surrounding each bead. The formula 5.1 simply justifies using $\alpha$ as a scalar metric and equivalent to the loss tangent for power law fluids. Furthermore, the predictor-corrector method is most robust in estimation of $\alpha$ faithfully distinguishing local sol-like versus gel-like behavior. *Nonetheless, using only* $\alpha$ *as a classifier does a remarkably good job of predicting the clusters of beads within each sample, whereas* $\tilde{D}_\alpha$ *basically plays the role of a corrector in singling out the few flake-like beads with values of* $\alpha$ *that could have been classified as*

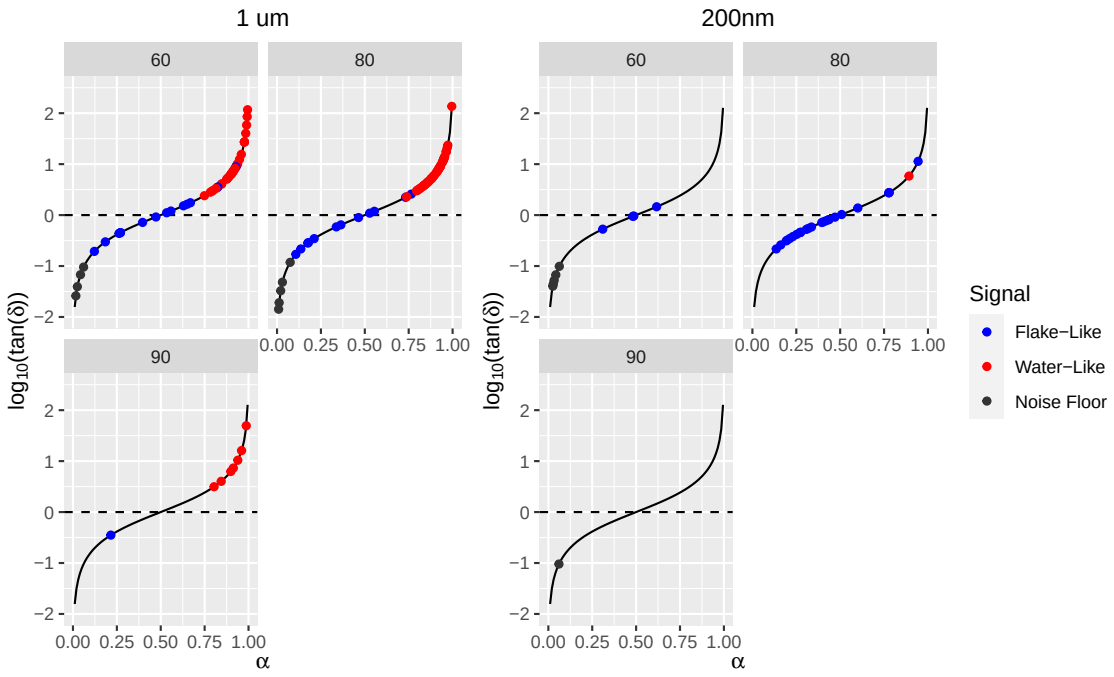


Figure 5.8: $\log_{10}(tan(\delta)) = \log_{10}(tan(\alpha/2))$ plots for 1um (left) and 200 nm (right) beads in HBE + CaLu3 mucus samples 60, 80, 90. Dots correspond to the scalar loss tangent metric per bead, the thin black curve is a plot of the function $\log_{10}(tan(\alpha/2))$, the black dashed horizontal line signals the sol-gel boundary. Blue, red, black dots are from flake-like, water-like, noise floor clusters.

*water-like. This coarse scalar metric does not, of course, convey the moduli surrounding each bead.*

Next, having used the classifier $(\alpha, \tilde{D}_\alpha)$ to identify beads within flakes and distinguishable from the noise floor, the GSER can be used to infer the dynamic moduli of the local properties surrounding within-flake beads of both 200 nm and 1 micron diameter.

## 5.2 Inferences of flake rheological properties

The storage and loss moduli of within-flake beads not in the noise floor are computed per bead for all three samples and for both bead diameters. We then average G' and G" for each dataset, shown in Figure 5.9. The noise floor and outside-flake beads are discarded since we are only interested in properties of flakes. Averaging over beads with both above and below 0.5, and therefore weighted averages over power law functions $\omega^\alpha$, leads to potential sol-gel frequency transitions.

The 90% HBE, 10% MUC5AC sample only has 1 micron bead data within flakes. These data, consistent with Figures 1 and 2, indicate a clear gel rheology (almost all beads with $\alpha < 0.5$), with the storage modulus a half-decade above the loss modulus at all frequencies. We then find an expected rise in the moduli of 80% HBE, 20% MUC5AC. However, consistent with Figures 5.2 and 5.8 showing a balance of beads with $\alpha$

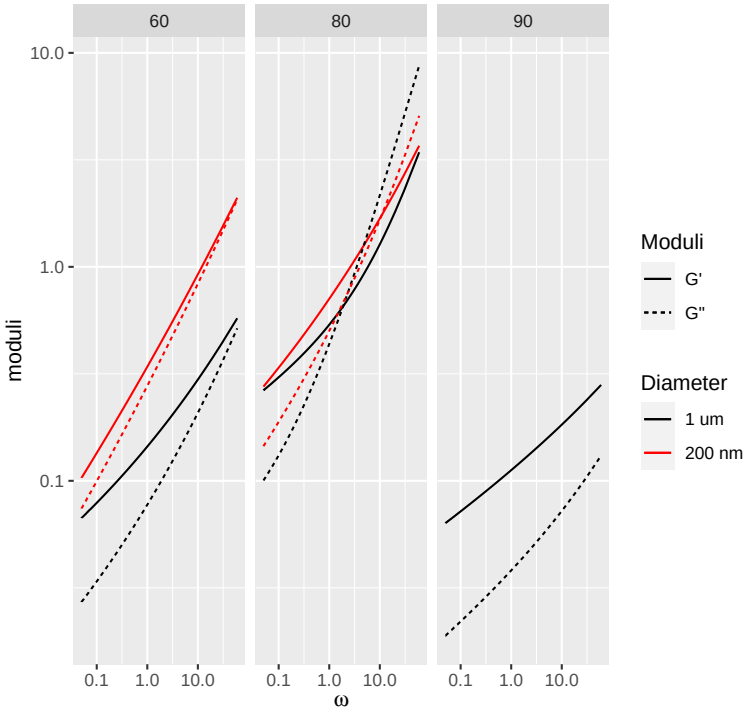


Figure 5.9: Plots showing the average storage and loss moduli for the within-flake and outside the noise floor clusters for one micron and 200 nm beads for each of the three samples, the same clusters identified in Figures 5.2, 5.8

above and below 0.5, the 80% HBE mucus is gel-like at low frequencies and sol-like at higher frequencies, in both the 200 nm and 1 micron data, with the gel-sol transition at approximately the same intermediate frequency. Then surprisingly, the data reveals a non-monotone behavior, consistent with the non-monotone pore structure deduced from Figure 5.2: a slight drop in the moduli of 60% HBE, 40% MUC5AC, falling to values between the 80% and 90% HBE mucus, with both the 200 nm and 1 micron data; furthermore, the 60% HBE returns to a gel rheology from both probe diameters, but not as strong of a gel as the 90% HBE sample.

### 5.3 fARMAs classifier's ability to coarse-grain location of beads

The diffusion parameters, $(\alpha, \tilde{D}_\alpha)$, are then used to determine how accurate they are in determining whether a bead is in flake vs out of flake. To do this, the beads are visually categorized as in or out of the flake at their initial positions, and this is compared to the signals from Figure 5.2. (Note only labels for half of the samples were available, hence the difference in the two figures)

Examining Figure 5.10, all but three of the beads appear to be accurately categorized: one in the 80% one micron sample has a flake-like signal but is visually out of a flake, one in the 90% one micron sample has a water-like signal but appears to be in a flake, and one in the 80% 200nm sample has a flake-like signal but is

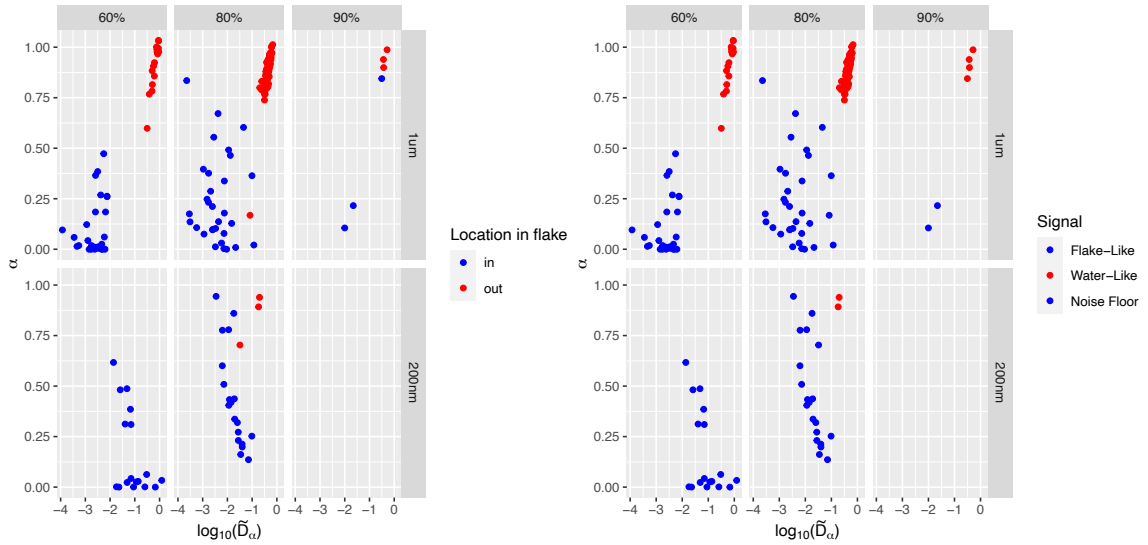


Figure 5.10: Plots of the same $(\alpha, \tilde{D}_\alpha)$ values but with color coming from visual classification of in or out of flake and signal from figure 5.2. All but three of the beads appear to have the same signal as their in/out of flake classification.

visually out of the flake.

On closer examination, the misclassified bead for the $1\mu m$ 80% sample appears to be on or near a black dot. This likely is another bead that was never declared and labeled; meaning that this bead is experiencing dual-particle interactions and should have been discarded in the proximity filter. In the $1\mu m$ 90% there are three beads in what appear to be an out of focus flake. The likely explanation for the bead being classified as in the flake instead of out is the bead being at a focal length different than the flake but appearing within it in two dimensions. There does appear to be a clear explanation for the 200 nm bead giving a flake-like signal.

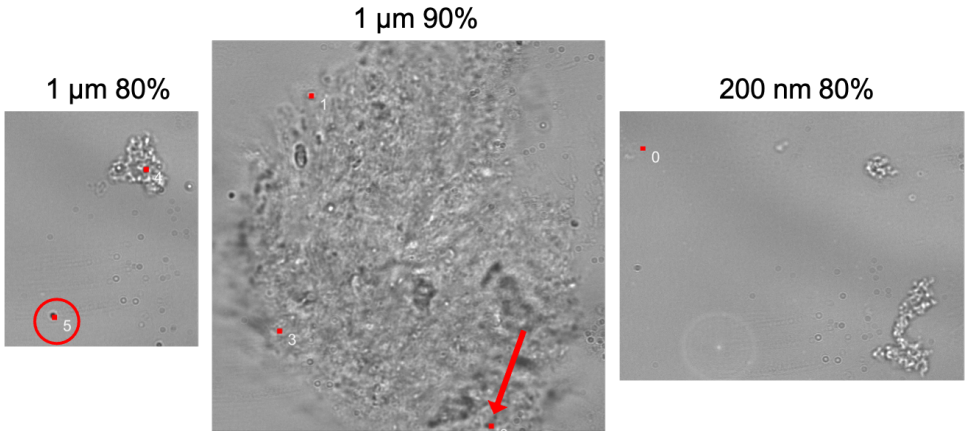


Figure 5.11: Images of the three incorrectly categorized beads in Figure 5.10

There are no other bodies in the vicinity to affect it like in the $1\mu m$ $80\%$ sample.

CHAPTER 6

# Conclusion

Analysis of the rheological and structural properties of mucosal flakes is forced to deal with two fundamental challenges: heterogeneity and entangling of the signal and noise.. Thus data analytics tools of passive particle tracking experimental data must be extended from standard homogeneous soft complex materials. The methods presented were developed to analyze PPTM data from reconstituted samples of pathological human bronchial epithelial (HBE) mucus. Specifically, tools were developed to assess two levels of heterogeneity: a coarse scale of dense, phase-separated, mucus flakes within a dilute solution of the remaining mucin polymers; then within flakes, beads for which the measured time series signal can versus cannot be confidently disentangled from the experimental noise floor.

For each tracked bead, a two-parameter classifier metric $(\alpha, D_\alpha)$ was developed by projecting the denoised signal onto fractional Brownian motion (fBm) using the entire experimental time series. The fBm classifier has been shown to be a robust statistical metric for passive particle tracking in HBE mucus [Wagner (2018), Hill (2014)]. For beads in flakes, however, previous statistical metrics for fitting fBm to time series data are inaccurate, as illustrated herein with synthetic data of noisy bead time series representative of tracked beads in dense flakes. The standard method for estimating diffusion parameters, least squares (LS), has no method to model or account for this signal-noise entanglement. Thus parametric models, with at least one parameter included to model noise, have been developed [Savin (2005), Lysy (2016)].

The classifier metric involves two steps, each utilizing bead time series: a predictor step based on a least squares fit to the mean-squared-displacement (MSD) of fBm, $MSD_X(n\tau) = 2dD_\alpha(n\tau)^\alpha$, giving an initial $(\alpha, D_\alpha)$ estimate which stabilizes the corrector step based on the fARMA method developed in [Ling (2021)]. To further improve the accuracy of the fARMA method for trajectories with significant levels the static noise, the fARMAs model, a hybrid of the fSD and fARMA models, was developed. *The method is shown here to accurately recover the truth in the same synthetic data for which previous metrics fail*.

Next, cluster analysis was performed in order to assess the two levels of heterogeneity in each of the three reconstituted samples of flake-burdened mucus. While the power law $\alpha$ is dimensionless, the MSD

pre-factor $D_\alpha$ has fractional, $\alpha$-dependent time units. Therefore in order to compare across beads or perform any clustering analysis the $D_\alpha$ parameter for each bead must be transformed to have either the same physical units, $\Delta$ (eq 1.7), or a common nondimensionalization, $\widetilde{D}_\alpha$ (eq 3.1). It should be emphasized that clustering is implemented on the denoised time series data, not on the complex moduli in frequency space after applying the generalized Stokes-Einstein relation (GSER). Once clustering is performed, the normality of the clusters is tested to justify either the single bead or ensemble-averaged GSER. *Experimental clusters are invariably non-normal, strongly suggesting within-cluster averaging post single-bead application of GSER*. Once the optimal GSER equation is determined, the dynamic moduli of flakes and dilute solution for each of the three samples that mimic progression of flake-prevalent mucus in cystic fibrosis are then computed.

The fBm classifier $(\alpha, D_\alpha)$ has another advantage. When applied to each tracked bead or the ensemble averaged classifier of approximately normal clusters, the fBm classifier has an exact power law mean-squared-displacement (MSD). Furthermore, the Fourier transform of a power law function is also exact and a power law function, so *the GSER applied either to individual bead classifiers, or to the ensemble average of classifiers, yields an exact power-law formula for the complex modulus, $G^*(\omega)$*. However, since all within-flake and outside-flake experimental clusters fail the test for homogeneity, within-cluster averaging of the power law moduli yields a non-power law cluster rheology. *The phase-separated mucus flakes clearly exhibit gel-dominated rheology over broad frequency ranges, whereas the dilute solution clearly exhibits sol-like rheology*. The within-flake data with both 200 nm and 1 micron diameter beads in samples from the same reconstituted batch also reveals probe-diameter dependent heterogeneity. This result is followed up with further analysis of flake structure within flakes, given the available data. By comparing the disparity between 1 $\mu$m and 200 nm diameter beads within flakes, it can be inferred that *the flake pore size is predominantly between 1 $\mu$m and 200 nm with some percentage of pores greater than 1 $\mu$m*.

## BIBLIOGRAPHY


1. T.G. Mason, D.A. Weitz, Optical measurements of frequency-dependent linear viscoelastic moduli of complex fluids, Phys Rev Lett 74: 1250 (1995)

2. T.G. Mason, K. Ganesan, J.H. vanZanten, D. Wirtz, S.C. Kuo, Particle tracking microrheology of complex fluids, Physical Review Letters 79: 3282 (1997)

3. T.G. Mason, Estimating the viscoelastic moduli of complex fluids using the generalized Stokes-Einstein equation, Rheologica Acta 39: 371 (2000)

4. J.V. Fahy, B.F. Dickey, Airway Mucus Function and Dysfunction, N. Engl. J. Med., 363 (23), 2233 2010

5. R. Bansil and B.S. Turner, The biology of mucus: Composition, synthesis and organization, Adv. Drug Deliv. Rev. 124, 3 (2018)

6. C.E. Wagner, K.M. Wheeler, K. Ribbeck, Mucins and their role in shaping the functions of mucus barriers, Annu. Rev. Cell Dev. Biol. 34, 189 (2018)

7. R.C. Boucher, Muco-obstructive lung diseases, N. Engl. J. Med. 380, 1941 (2019)

8. J.S. Crater, R.L. Carrier, Barrier Properties of Gastrointestinal Mucus to Nanoparticle Transport, Macromol. Biosci. 2010

9. D.B. Hill, S. McKinley, P. Vasquez, J. Mellnik, A. Vose, F. Mu, N. Alexis, R. Boucher, M.G. Forest, A biophysical basis for mucus solids concentration (wt%) as a candidate biomarker for airways disease: relationships to clearance in health and stasis in disease, PLoS ONE 9(2): e87681 (2014)

10. M. Lysy, N. Pillai, D.B. Hill, M.G. Forest, J. Mellnik, P. Vasquez, S.A. McKinley, Model comparison and assessment for single particle tracking in biological fluids, Journal of the American Statistical Association 111(516),1413 (2016)

11. C.E. Wagner, B.S. Turner, M. Rubinstein, G.H. McKinley, K. Ribbeck, A rheological study of the association and dynamics of MUC5AC gels, Biomacromolecules 18 (11), 3654 (2017)

12. D.B. Hill, R. Long, W. Kissner, E. Atieh, I. Garbarine, M. Markovetz, N. Fontana, M. Christy, M. Habibpour, R. Tarran, M.G. Forest, R. Boucher, B. Button, Pathological Mucus and Impaired Mucus Clearance in Cystic Fibrosis Patients Results from Increased Concentration, not altered pH, European Respiratory Journal 52, No. 6: 1801297 (2018)

13. J. Newby, A. Schaefer, P. Lee, M.G. Forest, S. Lai, Convolutional neural networks automate detection for tracking of submicron scale particles in 2D and 3D, Proceedings of the National Academy of Sciences 115(36) 9026 (2018)

14. C. Esther, M. Muhlebach, C. Ehre, D.B. Hill, M. Wolfgang, M. Kesimer, K. Ramsey, M. Markovetz, I. Garbarine, M.G. Forest, I. Seim, B. Zorn, C. Morrison, M. Delion, L. Turkovic, S. Ranganathan, S Stick, S. Conlan, R. Boucher, Mucus accumulation in the lungs precedes structural changes and infection in children with cystic fibrosis, Science Translational Medicine 11, Issue 486 (2019)

15. M. Markovetz, W. Kissner, I. Garbarine, C. Morrison, T. Kato, M. Papanikolas, R. Freeman, M.G. Forest, C. Esther Jr, M. Muhlebach, S. Stick, C. Ehre, R. Boucher, D. Hill, Establishing the Mucus Flake Burden as a Biomarker of CF Disease Severity, Pediatric Pulmonology, Wiley 111 River St, Hoboken 07030-5774, NJ USA (2019)

16. Y. Ling, M. Lysy, I. Seim, J. Newby, D. Hill, J. Cribb, M. G. Forest, Measurement error correction in particle tracking microrheology, Annals of Applied Statistics, 16(3): 1747-1773 DOI: 10.1214/21-AOAS1565 (2022)

17. A.J. Levine, T.C. Lubensky, One- and Two-Particle Microrheology, Phys. Rev. Lett. 85, 1774 (2000)

18. C. Hohenegger, M.G. Forest, Two-point microrheology: modeling protocols, Phys. Rev. E 78, 031501 (2008)

19. J.C. Crocker, M. T. Valentine, Eric R. Weeks, T. Gisler, P. D. Kaplan, A. G. Yodh, and D. A. Weitz, Two-Point Microrheology of Inhomogeneous Soft Materials," Phys. Rev. Lett. 85, 888 (2000)

20. M.T. Valentine, Z.E. Perlman, M.L. Gardel, J.H. Shin, P. Matsudaira, T.J. Mitchison, D.A. Weitz, Colloid surface chemistry critically affects multiple particle tracking measurements of biomaterials, Biophys J. 86(6):4004 (2004)

21. A. Ford, X. Cao, M. Papanikolas, M. Markovetz, D.B. Hill, T. Kato, R. Boucher, R. Freeman, M.G. Forest, Molecular dynamics simulations to explore the structure and rheological properties of normal and hyper-concentrated airway mucus, Studies in Applied Mathematics 147(4), 1369 (2021)

22. M. Markovetz, I.C. Garbarine, C.B. Morrison, W.J. Kissner, I. Seim, M.G. Forest, M.J. Papanikolas, R. Freeman, A. Ceppe, A. Ghio, N.E. Alexis, S.M Stick, C. Ehre, R.C. Boucher, C.R. Esther, M.S. Muhlebach, D.B. Hill, Mucus and mucus flake composition as candidate biomarkers of CF airway disease progression, Journal of Cystic Fibrosis 21(6):959 (2022)

23. K. Zhang, K. Crizer, M. Schoenfisch, D.B. Hill, G. Didier, Fluid heterogeneity detection based on the asymptotic distribution of the time-averaged mean squared displacement in single particle tracking experiments, Journal of Physics A: Mathematical and Theoretical (2018)

24. G. Sikora, K. Burnecki, A. Wyomaska, Mean-squared-displacement statistical test for fractional Brownian motion, Rev. E 95, 032110 (2017)

25. M. Backlund, W.E. Moerner, "Motion of chromosomal loci and the mean-squared displacement of a fractional Brownian motion in the presence of static and dynamic errors," Proc. SPIE 9331, Single Molecule Spectroscopy and Super-resolution Imaging VIII, 933106 (2015)

26. M. Backlund, R. Joyner, W.E. Moerner, Chromosomal locus tracking with proper accounting of static and dynamic errors, Phys. Rev. E 91, 062716 1-12 (2015) (DOI: 10.1103/PhysRevE.91.062716 (2015).

27. T. Savin, P. Doyle, Static and Dynamic Errors in Particle Tracking Microrheology, Biophysical Journal, Volume 88, Issue 1, Pages 623, ISSN 0006-3495 (2005)

28. W.G. Cochran, Problems arising in the analysis of a series of similar experiments, J R Stat Soc Suppl. 4:102 (1937)

29. W.G. Cochran, The combination of estimates from different experiments, Biometrics 10:101 (1954)

30. R.E. Kass, A.E. Raftery, "Bayes Factors" (PDF). Journal of the American Statistical Association. 90 (430): 791 (1995)

31. G. Didier, K. Zhang, The Asymptotic Distribution of The Pathwise Mean Squared Displacement in Single Particle Tracking Experiments, Journal of Time Series Analysis, 38(3):395 (2016)

32. Scrucca L, Fop M, Murphy TB, Raftery AE (2016). mclust 5: clustering, classification and density estimation using Gaussian finite mixture models. The R Journal, 8(1), 289

33. A. Allen, G. Flemstrom, A. Garner, E. Kivilaakso, Gastroduodenal mucosal protection,Physiological Reviews. 73 (1993) 823857

34. A. Silberberg, Rheology of mucus, mucociliary interaction, and ciliary activity, CellMotility. 2 (1982) 2528.

35. D.F. Katz, Human cervical mucus: Research update, American Journal of Obstetrics andGynecology. 165 (1991) 19841986.

36. D.J. Thornton, J.K. Sheehan, From Mucins to Mucus, Proc Am Thorac Soc. 1 (2004) 5461. https://doi.org/10.1513/pats.2306016; D.J. Thornton, K. Rousseau, M. McGuckin.Structure and function of the polymeric mucins in airways mucus. Annu Rev Physiol 70:459486, 2008.